Simulating laser-fluid coupling and laser-induced cavitation using embedded boundary and level set methods

Xuning Zhao, Wentao Ma, Kevin Wang *

Kevin T. Crofton Department of Aerospace and Ocean Engineering, Virginia Tech, Blacksburg, VA 24061, USA

A B S T R A C T

A computational method for simulating thermal cavitation induced by long-pulsed laser is presented. This method accounts for the absorption of laser light by a liquid, the formation of vapor bubbles due to localized heating, and the dynamics of the bubbles and the surrounding liquid. The physical model combines the Euler equations for a compressible inviscid two-phase fluid flow, a reduced form of the radiative transfer equation for laser radiation, and a local thermodynamic model of vaporization. The Euler equations are solved using the FInite Volume method with Exact two-phase Riemann solvers (FIVER). Following this method, numerical fluxes across phase boundaries are computed by constructing and solving one-dimensional bimaterial Riemann problems. The paper focuses on numerical methods for coupling the laser and fluid governing equations and tracking the vapor bubbles. An embedded boundary finite volume method is proposed to solve the laser radiation equation on the same mesh created for the Euler equations, which usually does not resolve the boundary and propagation directions of the laser beam. To impose boundary conditions, ghost nodes outside the laser domain are populated by mirroring and interpolation techniques. The existence and uniqueness of solution are proved for the two-dimensional case, leveraging the special geometry of the laser domain. The order of accuracy of the method is also proved, and verified using numerical tests. A method of latent heat reservoir is proposed to predict the onset of vaporization, which accounts for the accumulation and release of latent heat. A unique challenge associated with long-pulsed laser is that the dynamics of vapor bubbles is driven not only by the inertia of the bubble nuclei, but also by the continuation of vaporization. In this work, the localized level set method is employed to track the bubble surface, and a method of local correction and reinitialization is proposed to account for continuous phase transitions. Several numerical tests are presented to verify the convergence of these methods. Two realistic simulations of laser-induced cavitation are presented at the end, showing that the computational method is able to capture the key phenomena in these events, including non-spherical bubble expansion, shock waves, and the "Moses effect".

1. Introduction

Laser-induced cavitation describes the formation of vapor bubbles in a liquid due to laser radiation. As a mechanism of bubble generation, it is widely used in basic research and microfluidic applications that require controlled bubble dynam-

---

ics [1–6]. As a natural phenomenon, laser-induced cavitation also occurs in a broad range of applications that utilize laser to treat materials in a liquid environment. Examples in this category include liquid-assisted laser processing (e.g., underwater laser cutting [7,8], laser cleaning [9,10]), ocular laser surgery [11], laser angioplasty [12], and laser lithotripsy [13–16]. In many cases, cavitation is a major complexity, as it produces both beneficial and detrimental effects [16–18]. Therefore, understanding laser-induced cavitation and the subsequent bubble dynamics is crucial to improving the efficacy and safety of these technologies.

The duration of a laser pulse varies from 10^{-15} s to 1 s or longer in different applications. If the pulse duration is much smaller than the acoustic time scale (i.e. characteristic length divided by the speed of sound in the liquid), laser radiation can be viewed as a preceding event that stops before the vapor (or plasma) bubble starts to expand. In this case, the analysis of bubble and fluid dynamics can be separated from that of laser radiation. If the pulse duration is comparable to or longer than the acoustic time scale (i.e. long-pulsed laser), it may overlap with the expansion of the initial bubble. As a result, the dynamics of the bubble may be driven not only by the inertia of the initial bubble, but also by the continuation of phase transition. In practice, an evidence of this phenomenon is the observation of a non-spherical bubble that reflects the direction and profile of the laser beam [14,19–21]. In this scenario, laser radiation, phase transition (e.g., vaporization), and the dynamics of the bubble and the surrounding liquid are interdependent, and should be analyzed as a combined system. In this paper, we present a computational method for conducting this type of analysis.

Existing models of bubble dynamics can be roughly divided into three categories, namely the Rayleigh-Plesset equation and its variants (e.g., [22–24]), the boundary potential equation (e.g., [25–27]), and two-phase Euler and Navier-Stokes equations (e.g., [28–32]). Analyses based on these models typically start with one or multiple pre-specified bubbles with a constant initial state inside each bubble. For bubbles generated by long-pulsed laser, this approach is no longer applicable due to the continuation of laser radiation and phase transition. To our knowledge, a full-domain method that predicts continuous, laser-induced phase transitions together with the two-phase bubble/fluid dynamics has not been presented in the literature. This paper presents an effort towards filling this gap. We couple the two-phase Euler equations with a laser radiation equation that models the absorption of laser light by the two-phase fluid flow. The laser radiation equation is obtained by customizing the radiative transfer equation (RTE) using the special properties of laser beams, including monochromaticity, directionality, and a measurable (often non-zero) focusing or diverging angle. The coupled fluid-laser system accounts for the continuous absorption of laser by the fluid flow before and after bubble formation, as well as the effect of temperature variation and bubble dynamics on laser attenuation.

To solve the two-phase Euler equations, we employ the FInite Volume method with Exact two-phase Riemann solvers (FIVER), which has been validated for several laboratory experiments on inertial and shock-induced bubble dynamics [29, 30,33]. Following this method, the mass, momentum, and energy fluxes across the liquid-vapor interface are computed by constructing and solving one-dimensional bimaterial Riemann problems [33–36]. In this way, the discontinuity of equation of state across the material interface is directly accounted for in the fluxes. We propose to solve the laser radiation equation using the same finite volume mesh created for the fluid equations (i.e. Euler equations). Compared to previous studies that solve fluid equations and the RTE on different meshes [37–39], the proposed approach reduces the amount of work by the user on mesh generation and partition. It also eliminates the need of frequent, full-domain data transfer between two meshes, which can be complex and expensive in massively parallel computations. In most cases, only a fraction of the fluid domain is subjected to laser radiation, which means the boundaries of the laser radiation domain are embedded inside the fluid domain, and not resolved by the fluid mesh. To account for this complexity, we apply an embedded boundary method to impose the boundary conditions of the laser radiation equation. Specifically, we populate ghost nodes outside the laser domain using mirroring and interpolation techniques. This method has been widely used in fluid-structure interaction computations, sometimes also referred to as ghost cell or immersed boundary method [40–44]. If the embedded boundary has an arbitrary geometry, the image of a ghost node may not be unique, and the local interpolation problem may be under-determined. In this work, we prove for the two-dimensional case that for the special geometry of the laser radiation domain, the solution of the embedded boundary method exists and is unique.

To capture laser-induced vaporization, we propose a method of latent heat reservoir that accounts for the accumulation and release of latent heat. For each control volume in the liquid subdomain, an additional variable is introduced to store the latent heat required to break up the intermolecular bonds. The transition from liquid to vapor phase is realized numerically by switching the equation of state to that of the vapor phase, then adding the latent heat to the enthalpy of the vapor through an isochoric process. To track the bubble surface (i.e. liquid-vapor interface), we apply a localized level set method that solves the level set equation within a narrow band that contains the interface [45]. In the past, the level set method has been widely used to track the evolution of bubbles driven by the fluid velocity field (i.e. advection) [29,30,33,46–49]. To capture the effect of continuous vaporization, we switch the sign of the level set function value within control volumes that have just undergone a phase transition. Then, we solve the level set reinitialization equation [46] to restore the level set function to a signed distance function.

To demonstrate and assess the capabilities of the proposed computational method, we present six numerical experiments. Among them, there are four academic benchmark problems that are used to verify the convergence and/or order of accuracy of the aforementioned numerical methods. The last two numerical experiments are realistic simulations of laser-induced cavitation. In these simulations, we vary the width of the laser beam, and show that the computational method is able to capture several key phenomena that have been discovered in laboratory experiments, including non-spherical, beam-
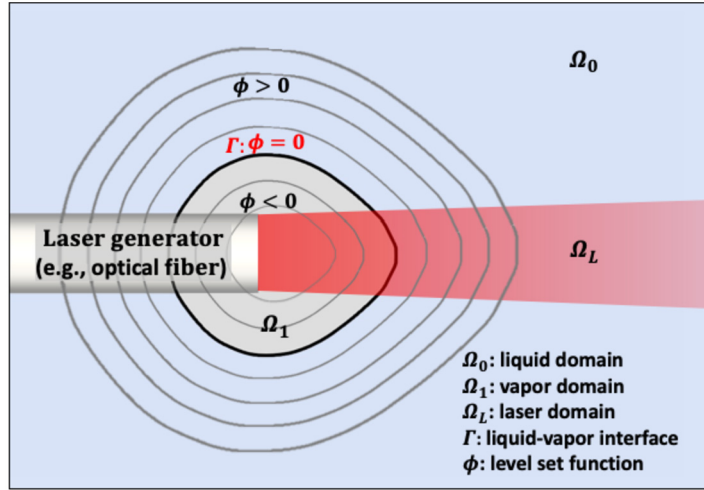
Fig. 1. Problem setup.

dependent bubble expansion, the emission of acoustic and shock waves, and the formation of a bubble channel that extends the range of laser radiation, also known as "Moses effect" [14,21,50,51].

2. Physical model

2.1. Fluid dynamics and thermodynamics

Fig. 1 provides an illustration of the problem investigated in this paper. As the cavitation bubble nucleates and expands, the fluid flow is dominated by high pressure, shock waves, and rapid interface motion. In comparison, viscous stresses and surface tension can be neglected. The effect of heat diffusion is also neglected in this work, as we focus on thermal radiation and advection. Based on these assumptions, the dynamics of the fluid flow is governing by the following Navier-Stokes equations.

$$\frac{\partial \boldsymbol{W}(\boldsymbol{x}, t)}{\partial t} + \nabla \cdot \mathcal{F}(\boldsymbol{W}) = \nabla \cdot \mathcal{G}(\boldsymbol{W}), \qquad \forall \boldsymbol{x} \in \Omega,\ t > 0, \tag{1}$$

with

$$\boldsymbol{W} = \begin{bmatrix} \rho \\ \rho \boldsymbol{V} \\ \rho e_t \end{bmatrix}, \qquad \mathcal{F} = \begin{bmatrix} \rho \boldsymbol{V}^T \\ \rho \boldsymbol{V} \otimes \boldsymbol{V} + p\boldsymbol{I} \\ (\rho e_t + p)\boldsymbol{V}^T \end{bmatrix}, \qquad \mathcal{G} = \begin{bmatrix} \boldsymbol{0}^T \\ \boldsymbol{0} \\ -\boldsymbol{q_r}^T \end{bmatrix},$$

where $\Omega \subset \mathcal{R}^3$ is the domain of the fluid flow, assumed to be time-independent. ρ, $\boldsymbol{V}$, p, T denote the fluid's density, velocity, pressure, and temperature, respectively. e_t is the total energy per unit mass (dimension: [length]^2[time]$^{-2}$), given by

$$e_t = e + \frac{1}{2}|\boldsymbol{V}|^2, \tag{2}$$

where e denotes the fluid's internal energy per unit mass. $\boldsymbol{q_r}$ is the radiative heat flux (dimension: [mass][time]$^{-3}$[length]$^{-1}$), assumed to be induced by laser. Therefore, Eq. (1) can be viewed as an extension of Euler equations to include thermal radiation.

To model a multiphase flow, we assume that one equation of state (EOS) is specified for each phase. In this work, we consider a two-phase flow involving the liquid and vapor phases. Thus, the EOS can be written as

$$p = p(\rho, e, \mathcal{I}) = \begin{cases} p_0(\rho, e), & \text{if } \mathcal{I} = 0, \\ p_1(\rho, e), & \text{if } \mathcal{I} = 1, \end{cases} \tag{3}$$

where $\mathcal{I} = \mathcal{I}(\boldsymbol{x}, t) \in \{0, 1\}$ denotes the phase (or material) identification number, $p_0(\rho, e)$ is the EOS of the liquid, and $p_1(\rho, e)$ the EOS of the vapor.

In the numerical tests presented in this paper, the stiffened gas EOS,

$$p_0(\rho, e) = (\gamma_0 - 1)\rho e - \gamma_0 p_{c0}, \tag{4}$$

is applied to model the liquid, and the (calorically) perfect gas EOS,

$$p_1(\rho, e) = (\gamma_1 - 1) \rho e, \tag{5}$$

is applied to model the vapor. Here, γ_0, p_{c0}, and γ_1 are material-dependent parameters.

To properly model laser absorption, a temperature law is also needed for each phase. For the two-phase flow, the temperature law can be written as

$$T = T(h, \mathcal{I}) = \begin{cases} T_0(h), & \text{if } \mathcal{I} = 0, \\ T_1(h), & \text{if } \mathcal{I} = 1, \end{cases} \tag{6}$$

where $h = e + p/\rho$ denotes enthalpy. $T_0(h)$ and $T_1(h)$ are the temperature laws of the liquid and vapor phases, respectively. In the numerical tests presented in this paper, we assume

$$T_1(h) = \frac{1}{c_{p1}} (h - h_{c1}) + T_{c1}, \tag{7}$$

for the vapor phase, where h_{c1} and T_{c1} represent a reference state, and c_{p1} is the specific heat at constant pressure, assumed to be a constant. For the liquid phase modeled using the stiffened gas EOS, we also assume a constant c_p, which gives

$$T_0(h) = \frac{1}{c_{p0}} (h - h_{c0}) + T_{c0}. \tag{8}$$

2.2. Liquid-vapor interface

At any time $t \geq 0$, the subdomains occupied by the liquid and the vapor are given by

$$\Omega_0(t) = \mathcal{I}_t^{-1}(0), \tag{9}$$

$$\Omega_1(t) = \mathcal{I}_t^{-1}(1), \tag{10}$$

where $\mathcal{I}_t^{-1}$ denotes the inverse function of $\mathcal{I}$ at time t.

The liquid-vapor interface, Γ, is therefore given by

$$\Gamma(t) = \partial \Omega_0(t) \cap \partial \Omega_1(t). \tag{11}$$

The interface conditions imposed in this work are those describing a contact discontinuity, i.e.,

$$\begin{aligned} \left(\lim_{\boldsymbol{x}' \to \boldsymbol{x}, \, \boldsymbol{x}' \in \Omega_0} \boldsymbol{V}(\boldsymbol{x}', t) - \lim_{\boldsymbol{x}' \to \boldsymbol{x}, \, \boldsymbol{x}' \in \Omega_1} \boldsymbol{V}(\boldsymbol{x}', t) \right) \cdot \boldsymbol{n}(\boldsymbol{x}, t) = 0, \\ \lim_{\boldsymbol{x}' \to \boldsymbol{x}, \, \boldsymbol{x}' \in \Omega_0} p(\boldsymbol{x}', t) = \lim_{\boldsymbol{x}' \to \boldsymbol{x}, \, \boldsymbol{x}' \in \Omega_1} p(\boldsymbol{x}', t), \end{aligned} \qquad \forall \boldsymbol{x} \in \Gamma, \, t \geq 0, \tag{12}$$

where $\boldsymbol{n}$ denotes the normal to Γ.

We track Γ implicitly by solving the level set equation,

$$\frac{\partial \phi}{\partial t} + \boldsymbol{V} \cdot \nabla \phi = 0, \tag{13}$$

where ϕ is the level set function, initialized to be the signed shortest distance to the interface. We adopt the convention that the positive sign of ϕ corresponds to the liquid phase. In this way, Ω_0, Ω_1, and Γ are given by

$$\Omega_0(t) = \{\boldsymbol{x} \in \Omega, \, \phi(\boldsymbol{x}, t) > 0\}, \tag{14}$$

$$\Omega_1(t) = \{\boldsymbol{x} \in \Omega, \, \phi(\boldsymbol{x}, t) < 0\}, \tag{15}$$

$$\Gamma(t) = \{\boldsymbol{x} \in \Omega, \, \phi(\boldsymbol{x}, t) = 0\}. \tag{16}$$

Combining Eqs. (9), (10), (14) and (15), the phase identification function $\mathcal{I}$ can also be derived using the level set function ϕ.

For problems in which the liquid-vapor interface emerges after the start of the computation (i.e. at some $t > 0$), we begin solving Eq. (13) after the interface emerges, while the fluid governing equations (1) are always solved from $t = 0$. At the end of each time step, a phase transition model is applied to check the thermodynamic state variables at each node and identify possible phase transitions. For each node that undergoes phase transition (e.g., vaporization), the local value of ϕ is reset to a small value that has the sign corresponding to the phase it transitions into (e.g., vapor). In this work, the magnitude of ϕ is set to be half of the minimum edge length within a neighborhood of the node. After this manipulation,

ϕ has the correct sign at every node, but it is no longer a distance function. We restore ϕ to a signed distance function by solving the reinitialization equation [46],

$$\frac{\partial \phi}{\partial \tilde{t}} + S(\phi_0)(|\nabla \phi| - 1) = 0, \tag{17}$$

to the steady state, which satisfies $|\nabla \phi| = 1$. Here, $\tilde{t}$ is a fictitious time variable. ϕ_0 is the level set function before reinitialization. $S(\phi_0)$ is a smoothed sign function, given by

$$S(\phi_0) = \frac{\phi_0}{\sqrt{\phi_0^2 + \varepsilon^2}}, \tag{18}$$

where ε is a constant coefficient, set to the minimum element size of the mesh. The steady state solution of Eq. (17) is then used as the new initial condition to integrate the level set equation (13) forward in time. Details of the phase transition model and the implementation method are presented in Sec. 2.4 and Sec. 3.5.

The phase transition method described above requires frequent solution of Eq. (17). To reduce the computational cost, we employ the localized level set method [45], which means Eq. (13) is solved within a subset of Ω that contains points within a certain bandwidth (in terms of mesh connectivity) from the zero level set. In this way, Eq. (17) only needs to be solved within a narrow band that is slightly wider than the domain of Eq. (13). The localized domains of Eqs. (13) and (17) are both updated at every time step.

2.3. Laser radiation

Let $\Omega_L \subset \Omega$ be the region inside the fluid domain that is subjected to laser radiation (Fig. 1). In general, the transfer of laser energy within Ω_L is governed by the law of energy conservation [52], which can be written in an integral form as

$$\int_{\partial V} (L\hat{s}) \cdot \mathbf{n} dA = \int_V \left(\mu_\alpha(\eta) L_b(\mathbf{x}, \eta) - \mu_\alpha(\eta) L(\mathbf{x}, \hat{s}, \eta) - \mu_s(\eta) L(\mathbf{x}, \hat{s}, \eta) + \frac{\mu_s(\eta)}{4\pi} \int_{4\pi} L(\mathbf{x}, \hat{s}_i, \eta) \Phi(\hat{s}_i, \hat{s}) d\omega_i \right) dV, \tag{19}$$

where $V \subset \Omega_L$ denotes an arbitrary control volume, and ∂V its boundary. $\mathbf{n}$ denotes the unit normal to ∂V. $L = L(\mathbf{x}, \hat{s}, \eta)$ denotes the spectral radiance (dimension: [mass][time]$^{-3}$[length]$^{-1}$) at position $\mathbf{x} \in \mathcal{R}^3$, along direction $\hat{s}$, at wavelength η. L_b denotes blackbody radiance. μ_α and μ_s are the absorption coefficient and the scattering coefficient, respectively, which depend on the laser wavelength and the medium. $\Phi(\hat{s}_i, \hat{s})$ is the scattering phase function, which describes the probability that a ray from one direction $\hat{s}_i$ would be scattered into another direction $\hat{s}$. ω denotes the solid angle.

Applying the Gauss theorem to Eq. (19) yields

$$\nabla \cdot (L\hat{s}) = \mu_\alpha(\eta) L_b(\mathbf{x}, \eta) - \mu_\alpha(\eta) L(\mathbf{x}, \hat{s}, \eta) - \mu_s(\eta) L(\mathbf{x}, \hat{s}, \eta) + \frac{\mu_s(\eta)}{4\pi} \int_{4\pi} L(\mathbf{x}, \hat{s}_i, \eta) \Phi(\hat{s}_i, \hat{s}) d\omega_i, \tag{20}$$

where ∇ denotes the gradient with respect to $\mathbf{x}$.

The radiative heat flux $\mathbf{q}_r$ in Eq. (1) is obtained by integrating L over all directions and the interval of relevant wavelengths, $(\eta_{\min}, \eta_{\max})$. That is,

$$\mathbf{q_r}(\mathbf{x}) = \int_{\eta_{\min}}^{\eta_{\max}} \int_{4\pi} L(\mathbf{x}, \hat{s}, \eta) \hat{s} \, d\omega d\eta. \tag{21}$$

If $\hat{s}$ is independent of $\mathbf{x}$, the left-hand side of Eq. (20) becomes $\nabla L \cdot \mathbf{s}$, which gives the well-known radiative transfer equation (RTE) [52,53].

The special properties of laser light allow us to simplify Eqs. (20) and (21). Because of monochromaticity, we can assume that L is non-zero only at a fixed laser emission wavelength, η_0. Compared with the high intensity of the laser light, the blackbody radiance due to emission of the medium is small enough to be neglected. Because of the directionality of the laser light, and ignoring the emission term, we can assume that L is non-zero only along the direction of laser propagation, denoted by $\mathbf{s}$. Hence,

$$L(\mathbf{x}, \hat{s}, \eta) = L(\mathbf{x})\delta(\hat{s} - \mathbf{s})\delta(\eta - \eta_0), \tag{22}$$

where $\delta(\cdot)$ denotes the delta function, and the variable $L(\mathbf{x})$ on the right-hand side is radiance (dimension: [mass][time]$^{-3}$).[1] It should be noted that $\mathbf{s}$ is not always a constant. In particular, if the laser beams are focusing or diverging − which is common in practice − $\mathbf{s}$ is a function of $\mathbf{x}$.

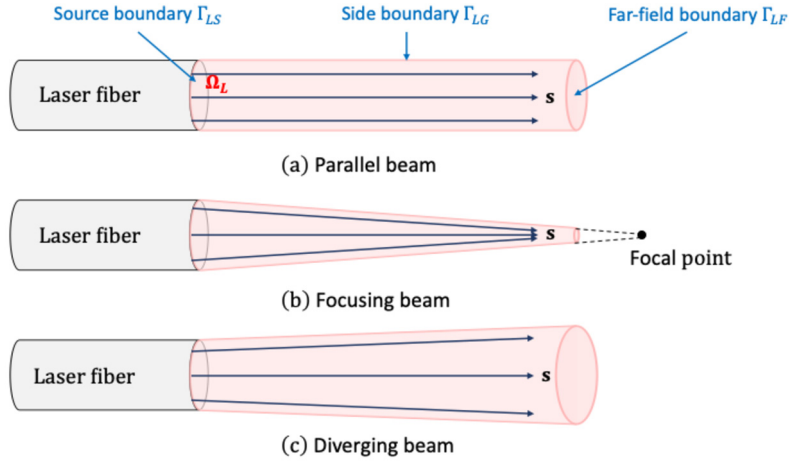[1] After this point, the variable L always denotes radiance.

Fig. 2. Laser domain geometries. For focusing beams, it is assumed that the focal point is excluded from the domain.

Substituting Eq. (22) into Eq. (20) and setting $L_b(\boldsymbol{x}, \eta) = 0$, we obtain

$$\nabla \cdot (L\boldsymbol{s}) = \nabla L \cdot \boldsymbol{s} + (\nabla \cdot \boldsymbol{s})L = -\mu_\alpha L, \tag{23}$$

where $L = L(\boldsymbol{x})$, and $\boldsymbol{s} = \boldsymbol{s}(\boldsymbol{x})$ is a known function. Similarly, substituting Eq. (22) into Eq. (21) yields

$$\boldsymbol{q}_r = L\boldsymbol{s}. \tag{24}$$

Considering the cases of parallel, focusing, and diverging laser beams, the domain of the laser radiation equation, Ω_L, can be a circular cylinder or a truncated cone (Fig. 2).

Let $\Gamma_L = \partial \Omega_L$, and $\Gamma_{LS} \subset \Gamma_L$ be the boundary that corresponds to the laser source. At the laser source, L can often be modeled using a Gaussian function [54] or set to a constant value, thereby providing a Dirichlet boundary condition. For a Gaussian beam,

$$L(\boldsymbol{x}) = L_0(r) = \frac{2P_0}{\pi w_0^2} \exp\left(\frac{-2r^2}{w_0^2}\right), \quad \forall \boldsymbol{x} \in \Gamma_{LS}, \tag{25}$$

where $r = \|\boldsymbol{x} - \boldsymbol{x}_0\|_2$ is the distance from point $\boldsymbol{x}$ to the center of the laser source, denoted by $\boldsymbol{x}_0$. P_0 and w_0 are model parameters corresponding to the power of the laser and the waist radius, respectively. P_0 can be a constant or a function of time t. Either way, it should be adjusted from the actual laser power to account for the fact that the Gaussian function is restricted to a finite domain.

The absorption coefficient μ_α is a function of both the material identification number $\mathcal{I}$ and temperature T. Therefore, the laser radiation equation (23), the fluid governing equation (1), and the level set equation (13) are interdependent.

2.4. Laser-induced vaporization

Due to the absorption of laser light, the temperature at any point within $\Omega_L \cap \Omega_0$ will increase following the temperature law defined in Sec. 2.1, until the vaporization temperature, T_{vap}, is reached at the point. After reaching T_{vap}, additional heat will not cause further temperature increase. Instead, it increases the material's intermolecular potential energy. In this work, we introduce a new variable, $\Lambda(\boldsymbol{x}, t)$ (dimension: [length]^2[time]$^{-2}$), to store this additional energy. Λ is initialized to 0 everywhere. At any point, it starts to increase only after the local temperature has reached T_{vap}.

Let l denote the material's latent heat of vaporization (dimension: [length]^2[time]$^{-2}$). When $\Lambda(\boldsymbol{x}, t)$ reaches l, a transition from the liquid phase to the vapor phase occurs at the point $\boldsymbol{x}$, which means $\boldsymbol{x}$ moves from Ω_0 into Ω_1. At the same time, the accumulated latent heat (Λ, which is equal to l) is released, and added to the enthalpy of the vapor. In an Eulerian reference frame, this is done through an isochoric process in order to satisfy mass conservation.

Specifically, for any point in Ω_L that undergoes phase transition, let ρ_0 and e_0 denote the density and internal energy at this point right before phase transition. After phase transition, the density at this point remains ρ_0, while the internal energy, e, is given by

$$e + \frac{p_1(\rho_0, e)}{\rho_0} = e_0 + \frac{p_0(\rho_0, e_0)}{\rho_0} + \Lambda, \tag{26}$$

where $p_0(\cdot, \cdot)$ and $p_1(\cdot, \cdot)$ are the EOS of the liquid and vapor phases, respectively (see Sec. 2.1). Depending on the choices of EOS, e can be solved from Eq. (26) analytically or numerically.
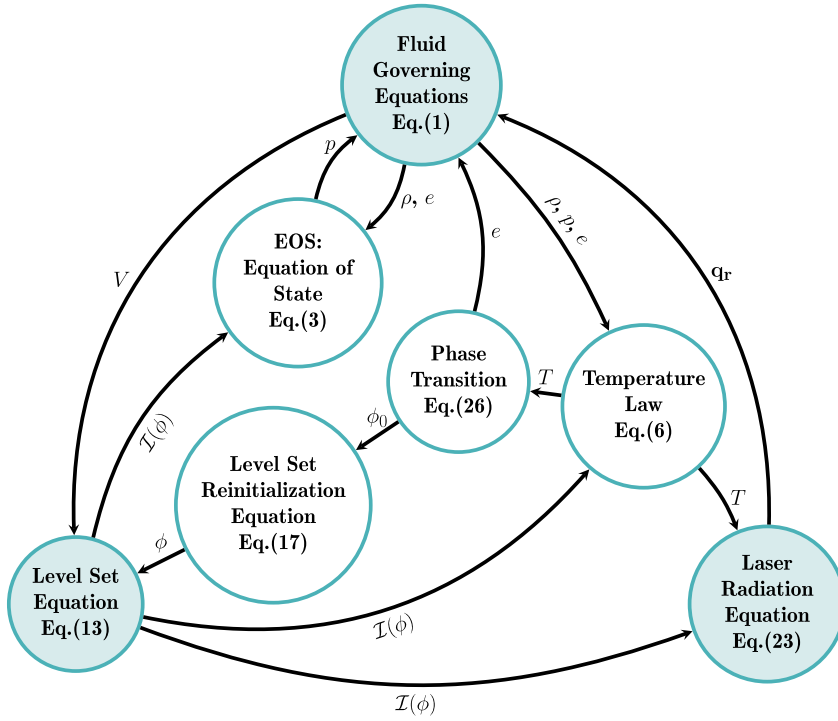
Fig. 3. Dependencies of the model equations.

This method is referred to as a method of latent heat reservoir in this paper, as Λ can be viewed as a reservoir that accumulates the latent heat of vaporization. It takes T_{vap} and l as input parameters, which can be constants or functions. The method is similar to those presented in [55] and [56], despite that fluid dynamics equations are not solved there.

As a summary, Fig. 3 shows the dependencies of all the model equations. The numerical solution process starts with initializing the fluid density (ρ), velocity (V), and pressure (p) fields at time $t = 0$. If a bubble exists at this time, the level set function ϕ is initialized to be a signed distance function with the zero level set being the bubble surface. Otherwise, ϕ does not need to be initialized, as the level set equation solver will remain inactive until material interface appears. The fluid governing equations (1) and the level set equation (13) are integrated in time using the same time integrator. Within each time step, the exchange of data between different solver modules are indicated in Fig. 3.

3. Numerical methods

3.1. Solution of the fluid governing equations

Let Ω^h be a spatial discretization of the computational domain Ω (Fig. 4). Around each node $\boldsymbol{n}_i \in \Omega^h$, a control volume C_i is created. All the control volumes form the dual mesh.

Integrating Eq. (1) within C_i gives

$$\int_{C_i} \frac{\partial \boldsymbol{W}_h}{\partial t} d\boldsymbol{x} + \int_{C_i} \nabla \cdot \mathcal{F}(\boldsymbol{W}_h) d\boldsymbol{x} = \sum_{\substack{\boldsymbol{e} \in \mathcal{T}_h \\ i \in \boldsymbol{e}}} \int_{\boldsymbol{e}} \nabla \cdot \mathcal{G}(\boldsymbol{W}_h) N_i^{(\boldsymbol{e})}(\boldsymbol{x}) d\boldsymbol{x}, \tag{27}$$

where $\mathcal{T}_h$ denotes the set of elements in the mesh. $N_i^{(\boldsymbol{e})}(\boldsymbol{x})$ denotes a shape function in element $\boldsymbol{e}$ associated with node $\boldsymbol{n}_i$. The left-hand side of Eq. (27) is evaluated using a finite volume method. The right-hand side is computed using a finite element method. After spatial discretization, we obtain the semi-discrete form,

$$\frac{\partial \boldsymbol{W}_i}{\partial t} + \frac{1}{\| C_i \|} \sum_{j \in Nei(i)} \int_{\partial C_{ij}} \mathcal{F}(\boldsymbol{W}) \cdot \boldsymbol{n}_{ij} dS = \frac{1}{\| C_i \|} \sum_{\substack{\boldsymbol{e} \in \mathcal{T}_h \\ i \in \boldsymbol{e}}} \int_{\boldsymbol{e}} \nabla \cdot \mathcal{G}(\boldsymbol{W}_h) N_i^{(\boldsymbol{e})}(\boldsymbol{x}) d\boldsymbol{x}, \tag{28}$$

where $\boldsymbol{W}_i$ denotes the average of $\boldsymbol{W}$ in control volume C_i. $Nei(i)$ denotes the set of nodes connected to node $\boldsymbol{n}_i$ by a facet, $\partial C_{ij} = \partial C_i \cap \partial C_j$. $\boldsymbol{n}_{ij}$ is the unit normal to ∂C_{ij}. $\| C_i \|$ denotes the volume of C_i.
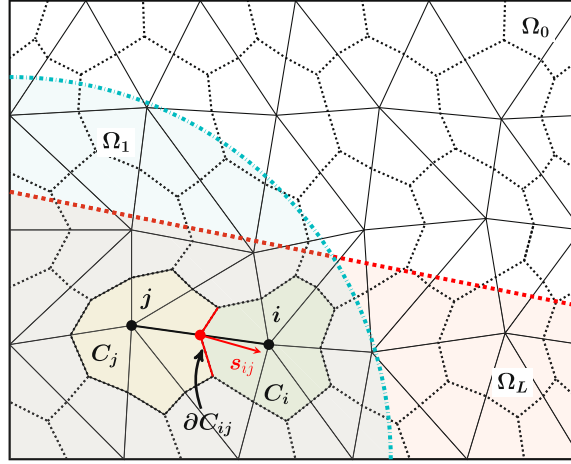
Fig. 4. 2D illustration of an arbitrary (i.e. unstructured) node-centered finite volume mesh. The elements of the primal mesh are shown in solid lines, while the control volumes that form the dual mesh are shown in dashed lines.

A second-order explicit Runge-Kutta method is used to integrate Eq. (28) in time. The FIVER method is used to calculate the fluxes across the facet ∂C_{ij} [29,30,33,57]. In this problem, based on the locations of node $\boldsymbol{n}_i$ and node $\boldsymbol{n}_j$, there are two possibilities:

(a) If $\boldsymbol{n}_i$ and $\boldsymbol{n}_j$ are in the same fluid subdomain, the well-known monotonic upstream-centered scheme for conservation laws (MUSCL) [58] is used to compute the fluxes across facet ∂C_{ij}.

(b) If $\boldsymbol{n}_i$ and $\boldsymbol{n}_j$ belong to different fluid subdomains (i.e. one in Ω_0 and the other in Ω_1), a one-dimensional bimaterial Riemann problem is constructed along the edge between $\boldsymbol{n}_i$ and $\boldsymbol{n}_j$, i.e.

$$\frac{\partial \boldsymbol{w}}{\partial \tau} + \frac{\partial \mathcal{F}(\boldsymbol{w})}{\partial \xi} = 0, \quad \text{with } \boldsymbol{w}(\xi, 0) = \begin{cases} \boldsymbol{w}_i, & \text{if } \xi \leq 0, \\ \boldsymbol{w}_j, & \text{if } \xi > 0, \end{cases} \tag{29}$$

where τ denotes the time coordinate. ξ denotes the spatial coordinate along the axis aligned with $\boldsymbol{n}_{ij}$ and centered at the midpoint between $\boldsymbol{n}_i$ and $\boldsymbol{n}_j$. The initial state $\boldsymbol{w}_i$ and $\boldsymbol{w}_j$ are given by projecting the states $\boldsymbol{W}_i$ and $\boldsymbol{W}_j$ onto the ξ axis. At any $\tau > 0$, the interface conditions (12) are satisfied by the solution of Eq. (29). For the stiffened gas and perfect gas EOS used in the numerical tests, Eq. (29) is solved analytically. The states to the left and right of the interface are used in the numerical flux function to compute the fluxes across the interface. In the test cases presented in this paper, the local Lax-Friedrichs flux (a.k.a. Rusanov flux) function is used, as it is simple and directly applicable to arbitrary EOS. The FIVER method has also been used in the past with other numerical flux functions, such as Roe, HLLE, and HLLC (e.g., [59]).

3.2. Solution of the level set equation and the reinitialization equation

The level set equation (13) can be solved using finite difference and finite volume methods on structured and unstructured meshes (e.g., [29,30,33,48,49]). In the numerical tests presented in this paper, the equation is solved using a third-order upwind finite difference method with a second-order explicit Runge-Kutta time-integrator.

When solving the level set reinitialization equation, it is difficult to restore ϕ to a signed distance function without causing any change to the location of the interface (i.e. the 0 level set of ϕ). This difficulty has led to different methods for updating the ϕ values at the first layer of nodes next to the interface (see, for example, [48,49]). We have implemented the constrained reinitialization methods presented in [49], referred to as HCR-1 and HCR-2, as well as a simple method that does not modify the ϕ values at the first layer of nodes (Eq. (39) in [48]). For the numerical tests presented in this paper, all the three methods produced similar and converging results.

3.3. Solution of the laser radiation equation

A finite volume method is implemented to solve the laser radiation equation. Integrating Eq. (23) within any control volume C_i, and applying the divergence theorem, we get

$$\sum_{j \in Nei(i)} A_{ij} L_{ij}(\boldsymbol{s}_{ij} \cdot \boldsymbol{n}_{ij}) = \int_{C_i} \nabla \cdot (L\boldsymbol{s}) d\boldsymbol{x} = -\int_{C_i} \mu_\alpha(T) L d\boldsymbol{x} = -\| C_i \| \mu_\alpha(T_i) L_i, \tag{30}$$

where A_{ij} is the area of facet ∂C_{ij}. L_i is the cell-average of L within C_i. L_{ij} is the value of L at facet ∂C_{ij}. $\boldsymbol{s}_{ij}$ denotes the laser direction at ∂C_{ij}. As shown in Fig. 4, $\boldsymbol{s}_{ij}$ is set to the laser direction at the midpoint between nodes $\boldsymbol{n}_i$ and $\boldsymbol{n}_j$.

A mean flux method (e.g., [60]) is applied to evaluate L_{ij}. For a node-centered finite volume formulation, L_{ij} is computed by

$$
L_{ij} = \begin{cases} \alpha L_i + (1-\alpha)L_j & \text{if } \boldsymbol{s}_{ij} \cdot n_{ij} \geq 0 \\ (1-\alpha)L_i + \alpha L_j & \text{if } \boldsymbol{s}_{ij} \cdot n_{ij} < 0 \end{cases}.
\tag{31}
$$

The value of parameter α can be varied between 0.5 and 1. When $\alpha = 1.0$, the resulting scheme is also referred to as the step method [60].

Substituting Eq. (31) into Eq. (30) yields a system of linear equations with the cell-averages of laser radiance as unknowns. Many linear solvers can be applied to solve this system. For example, using the Gauss-Seidel method, the iterative formula for updating L_i is given by

$$
L_i = -\frac{\alpha \sum\limits_{\substack{j \in Nei(i) \\ D_{ij} < 0}} A_{ij}D_{ij}L_j + (1-\alpha) \sum\limits_{\substack{j \in Nei(i) \\ D_{ij} \geq 0}} A_{ij}D_{ij}L_j}{\|C_i\|\mu_\alpha(T_i) + (1-\alpha)\sum\limits_{\substack{j \in Nei(i) \\ D_{ij} < 0}} A_{ij}D_{ij} + \alpha\sum\limits_{\substack{j \in Nei(i) \\ D_{ij} \geq 0}} A_{ij}D_{ij}},
\tag{32}
$$

where $D_{ij} = \boldsymbol{s}_{ij} \cdot \boldsymbol{n}_{ij}$.

Based on Eqs. (23) and (24), the divergence of the radiative flux, $\nabla \cdot \boldsymbol{q_r}$, is given by

$$
\nabla \cdot \boldsymbol{q_r} = \nabla \cdot (L\boldsymbol{s}) = -\mu_\alpha L.
\tag{33}
$$

Substituting Eq. (33) into the right-hand side of Eq. (28) yields

$$
\sum_{\substack{\boldsymbol{e} \in \mathcal{T}_h \\ i \in \boldsymbol{e}}} \int_{\boldsymbol{e}} \left(-\nabla \cdot \boldsymbol{q_r} \right)_h N_i(\boldsymbol{x}) d\boldsymbol{x} = \sum_{\substack{\boldsymbol{e} \in \mathcal{T}_h \\ i \in \boldsymbol{e}}} \int_{\boldsymbol{e}} \left(\mu_\alpha(T)L \right)_h N_i(\boldsymbol{x}) d\boldsymbol{x}.
\tag{34}
$$

3.4. Embedded boundary method

In general, the fluid mesh Ω^h does not contain a subset of nodes, edges, and elements that resolve the boundary of Ω_L or the laser propagation directions $\boldsymbol{s}(\boldsymbol{x})$. To handle this issue, an embedded boundary method is applied. We divide the boundaries of Ω_L into three parts, namely the source boundary (Γ_{LS}), the far-field boundary (Γ_{LF}), and the side boundary (Γ_{LG}) (Fig. 2). All of them can be embedded in the fluid mesh. The embedded boundary method can also be divided into three parts, as shown in Algorithms 1-1, 1-2, and 1-3.

First, we construct a label function $\mathcal{L}$ to identify whether the laser radiance at a node has been computed. Let $\mathcal{L}_i$ denote the label of node $\boldsymbol{n}_i$, which can be 0 or 1. At each time step, we initialize $\mathcal{L}$ as follows.

$$
\mathcal{L}_i = \begin{cases} 1, & \boldsymbol{x}_i \in \Omega_L, \\ 0, & \text{otherwise}, \end{cases}
\tag{35}
$$

where $\boldsymbol{x}_i$ denotes the coordinates of node $\boldsymbol{n}_i$. This is shown as Step 1 in Algorithm 1-1.

Algorithm 1-1: Embedded Boundary Method, Part I: Imposing the source condition.

---

1 **Step 1:** Initialize the label function $\mathcal{L}$

2 **for** $\forall \boldsymbol{n}_i \in \Omega^h$ **do**

3 $\quad$ $\mathcal{L}_i \leftarrow 1, \ \boldsymbol{x}_i \in \Omega_L$

4 $\quad$ $\mathcal{L}_i \leftarrow 0, \ \boldsymbol{x}_i \notin \Omega_L$

5 **end**

6 **Step 2:** Embed the source boundary Γ_{LS}

7 $\mathbb{N}_s \leftarrow \{\boldsymbol{n}_k \in \Omega^h \mid \boldsymbol{x}_k \in \Omega_{LS}\}$, where $\boldsymbol{x}_k$ is the coordinates of node $\boldsymbol{n}_k$

8 **for** $\forall \boldsymbol{n}_i \in \mathbb{N}_s$ **do**

9 $\quad$ **if** *Gaussian beam* **then**

10 $\quad\quad$ $L_i \leftarrow \dfrac{2P_0}{\pi w_0^2}\exp\left(-\dfrac{2r_i^2}{w_0^2}\right)$ (Eq. (25))

11 $\quad$ **else**

12 $\quad\quad$ $L_i \leftarrow L_c$ $\qquad\qquad\qquad\qquad\qquad\qquad\qquad\qquad\qquad\qquad\qquad$ $\triangleright$ L_c is a constant value for the radiance of the laser source

13 $\quad$ **end**

14 $\quad$ $\mathcal{L}_i \leftarrow 1$

15 **end**

For the source boundary Γ_{LS}, we consider a small region surrounding Γ_{LS} to be the laser source region. This region is defined by

$$\Omega_{LS} = \{\boldsymbol{x} \in \Omega \mid \mathcal{B}(\boldsymbol{x}, d_s) \cap \Gamma_{LS} \neq \emptyset\}, \tag{36}$$

where d_s is a small distance comparable to the characteristic element size of Ω^h, and $\mathcal{B}(\boldsymbol{x}, d_s)$ denotes the ball centered at $\boldsymbol{x}$ with radius d_s. All the nodes within Ω_{LS} are identified and stored in a set, $\mathbb{N}_s$. For any node $\boldsymbol{n}_i \in \mathbb{N}_s$, the laser radiance L_i is computed using the source condition, e.g., Eq. (25) for a Gaussian beam. Then, we set the label $\mathcal{L}_i = 1$. This is Step 2 in Algorithm 1-1.

To embed the side and far-field boundaries, we define the set of ghost nodes, $\mathbb{N}_G$, to include the first layer of nodes outside Ω_L whose label is still 0. For any ghost node $\boldsymbol{n}_i \in \mathbb{N}_G$, its projection point on $\partial\Omega_L$, denoted by $\boldsymbol{g}_i$, is defined to be the nearest point on $\Gamma_{LF} \cup \Gamma_{LG}$, i.e.

$$\boldsymbol{g}_i = \operatorname*{arg\,min}_{\boldsymbol{x} \in \Gamma_{LF} \cup \Gamma_{LG}} \|\boldsymbol{x} - \boldsymbol{x}_i\|_2. \tag{37}$$

We store the ghost nodes whose projection points are on Γ_{LF} in set $\mathbb{N}_f$, which corresponds to the far-field boundary. The others are stored in another set, $\mathbb{N}_g$, which corresponds to the side boundary. This is shown as Step 3 in Algorithm 1-2. Thus, we have

$$\mathbb{N}_f \cup \mathbb{N}_g = \mathbb{N}_G, \ \mathbb{N}_f \cap \mathbb{N}_g = \emptyset. \tag{38}$$

For the far-field boundary Γ_{LF}, we use a constant extrapolation method to populate the corresponding ghost nodes. For any node $\boldsymbol{n}_i \in \mathbb{N}_f$, the radiance L_i is set to be the same as its nearest neighbor within Ω_L. Then, the label $\mathcal{L}_i$ is set to 1. This is Step 4 in Algorithm 1-2. In practice, the far-field boundary should be sufficiently far from the laser source such that the radiance there is very low. Therefore, performing constant extrapolation near this boundary will have minimal effect on the overall solution accuracy.

Algorithm 1-2: Embedded Boundary Method, Part II: Identify ghost nodes.

---

17 **Step 3:** Identify ghost nodes
18 $\quad \mathbb{N}_G \leftarrow \{\boldsymbol{n}_k \in \Omega^h \mid \mathcal{L}_k = 0 \ \& \ \exists \boldsymbol{n}_j \in Nei(\boldsymbol{n}_k), \boldsymbol{x}_j \in \Omega_L\}$
19 **for** $\forall \boldsymbol{n}_i \in \mathbb{N}_G$ **do**
20 $\quad\quad$ Find $\boldsymbol{g}_i = \arg\min_{\boldsymbol{x} \in \Gamma_{LF} \cup \Gamma_{LG}} \|\boldsymbol{x} - \boldsymbol{x}_i\|_2$
21 **end**
22 $\quad \mathbb{N}_f \leftarrow \{\boldsymbol{n}_k \in \mathbb{N}_G \mid \boldsymbol{g}_k \in \Gamma_{LF}\}$
23 $\quad \mathbb{N}_g \leftarrow \{\boldsymbol{n}_k \in \mathbb{N}_G \mid \boldsymbol{g}_k \in \Gamma_{LG}\}$
24 **Step 4:** Embed the far-field boundary Γ_{LF}
25 **for** $\forall \boldsymbol{n}_i \in \mathbb{N}_f$ **do**
26 $\quad\quad L_i \leftarrow L_j, \ \text{with} \ \boldsymbol{x}_j = \arg\min_{\boldsymbol{n}_k \in \Omega_L} \|\boldsymbol{x}_k - \boldsymbol{x}_i\|_2$
27 $\quad\quad \mathcal{L}_i \leftarrow 1$
28 **end**

For the side boundary Γ_{LG}, we populate the corresponding ghost nodes to enforce a symmetric boundary condition, as shown in Step 5 in Algorithm 1-3. This ensures that there are no radiative fluxes crossing the side boundary, i.e.

$$\nabla L(\boldsymbol{x}) \cdot \boldsymbol{n} = 0, \quad \boldsymbol{x} \in \Gamma_{LG}, \tag{39}$$

where $\boldsymbol{n}$ is the outward unit normal of Γ_{LG}. To enforce this boundary condition, a mirroring method is used. We define the image point p_i for any ghost node $\boldsymbol{n}_i \in \mathbb{N}_g$ as

$$\boldsymbol{x}_{p_i} = 2\boldsymbol{g}_i - \boldsymbol{x}_i, \tag{40}$$

as shown on Lines $31 - 33$ in Algorithm 1-3. Then, a linear interpolation method is applied to compute the radiance at $\boldsymbol{x}_{p_i}$. In two-dimension (2D), there are three possibilities for the position of p_i.

(a) If $\boldsymbol{x}_{p_i}$ coincides with the position of a node within Ω_L, the radiance at the image is set to the radiance at this node.
(b) If $\boldsymbol{x}_{p_i}$ is on an edge of an element, the radiance is computed by linear interpolation along this edge.
(c) If $\boldsymbol{x}_{p_i}$ is inside an element, which must have at least one vertex within Ω_L, the radiance at the image is computed by linear interpolation within this element.

Thus, the radiance at $\boldsymbol{x}_{p_i}$ is given by

$$L(\boldsymbol{x}_{p_i}) = \begin{cases} L_j, & \text{if } \boldsymbol{x}_{p_i} = \boldsymbol{x}_j, \ \boldsymbol{x}_j \in \Omega_L \\ f_l(L_j, L_k), & \text{if } \boldsymbol{x}_{p_i} \in \partial\boldsymbol{e}_{jk} \\ f_l(L_j, L_k, L_l), & \text{if } \boldsymbol{x}_{p_i} \in \boldsymbol{e}_{jkl} \end{cases}, \tag{41}$$

where f_l denotes the linear interpolation function. ∂e_{jk} denotes an edge that connects nodes n_j and n_k. e_{jkl} denotes an element, assumed to be a triangle, that has n_j, n_k, and n_l as vertices.

This interpolation method can be easily extended to the three-dimensional (3D) case by including a new scenario in which the image point is inside a 3D element. For meshes that contain non-simplex elements, we recommend that the non-simplex elements first be divided into simplices (see the remark at the end of Sec. 3.4.1).

Next, the radiance at ghost node n_i is computed by

$$L_i = L(\boldsymbol{x}_{p_i}), \tag{42}$$

and we set the label $\mathcal{L}_i = 1$.

By Eqs. (37), (40), and (42), the symmetric boundary condition (Eq. (39)) is enforced on the side boundary of Ω_L.

Algorithm 1-3: Embedded Boundary Method, Part III: Mirroring and interpolation.

```
30   Step 5: Embed the side boundary Γ_LG
31   for ∀n_i ∈ N_g do
32   │   x_{p_i} ← 2g_i − x_i
33   end
34   while ∃ n_i ∈ N_g, L_i = 0 do
35   │   for n_i ∈ N_g do
36   │   │   if L_i = 0 then
37   │   │   │   if x_{p_i} = x_j then
38   │   │   │   │   L(x_{p_i}) ← L_j
39   │   │   │   else if x_{p_i} ∈ ∂e_jk then
40   │   │   │   │   L(x_{p_i}) ← f_l(L_j, L_k)
41   │   │   │   │   if ∃n_o ∈ {n_j, n_k}, x_o ≠ x_i & L_o = 0 then
42   │   │   │   │   │   continue
43   │   │   │   │   end
44   │   │   │   else
45   │   │   │   │   L(x_{p_i}) ← f_l(L_j, L_k, L_l), with {n_j, n_k, n_l} being the vertices of element e_jkl
46   │   │   │   │   if ∃n_o ∈ {n_j, n_k, n_l}, x_o ≠ x_i & L_o = 0 then
47   │   │   │   │   │   continue
48   │   │   │   │   end
49   │   │   │   end
50   │   │   │   L_i ← L(x_{p_i})
51   │   │   │   L_i ← 1
52   │   │   end
53   │   end
54   end
```

It should be noted that when populating ghost nodes, the interpolation may involve other ghost nodes within the same element that have not been populated yet. This means the equations in the second and third cases of Eq. (41) may be under-determined. Therefore, we need to keep iterating over all ghost nodes with label $\mathcal{L} = 0$. This is performed using the **while** loop in Algorithm 1-3.

3.4.1. Existence and uniqueness of solution

The mirroring and interpolation method described above has been employed in embedded/immersed boundary methods for solving fluid-structure interaction problems [40–44]. It should be noted that for an arbitrary surface embedded in a discretized spatial domain, Algorithm 1 may involve ambiguity or an infinite loop, which essentially means the solution of laser radiance at ghost nodes may either not exist, or be not unique. Fig. 5 shows two examples in 2D. Sub-figure (a) shows that when the subdomain enclosed by the embedded boundary is not convex, the image of a node may not be uniquely defined. In this scenario, Algorithm 1-2 would break at Line 20 due to ambiguity. Also, the **while** loop in Algorithm 1-3 may never terminate due to the existence of interdependent ghost nodes that cannot be populated. Sub-figure (b) shows that even if the embedded body is convex, the **while** loop may still be an infinite loop.

Nonetheless, because of the directionality of laser, the embedded laser radiation subdomain, Ω_L, is either a cylinder or a truncated cone (Fig. 2). Therefore, the image of any ghost node is uniquely defined by Eqs. (37) and (40). Next, we prove the existence of solution by showing that the **while** loop in Algorithm 1-3 cannot be an infinite loop. For this purpose, we assume that Ω^h is reasonably fine, such that the diameter of any transverse cross-section of Ω_L is greater than two times the maximum size of the elements in Ω^h that intersect this cross-section. Moreover, we assume that all the elements in Ω^h are simplices. Other types of elements can always be divided into simplices.

Proposition 1 *(Existence of solution). Under the conditions described above, Algorithm 1 terminates (i.e. $\mathcal{L}_i = 1$, $\forall n_i \in \mathbb{N}_g$) after a finite number of iterations.*
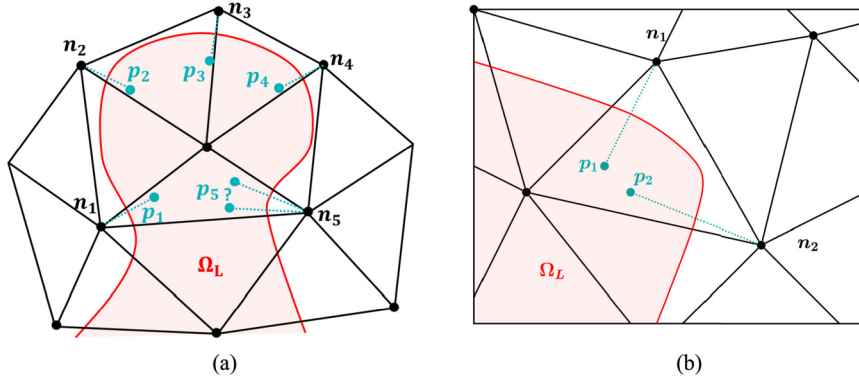
Fig. 5. Two examples in 2D showing that for an *arbitrary* boundary embedded in a mesh, the mirroring and interpolation method described in Algorithm 1 may involve ambiguity or an infinite loop. In example (a), the image of node $\boldsymbol{n}_5$ is not uniquely defined due to a non-convex embedded body. Also, $\mathcal{L}_i$, $1 \leq i \leq 5$ will remain 0, preventing the **while** loop from termination. In example (b), $\mathcal{L}_1$ and $\mathcal{L}_2$ will remain 0, leading to an infinite **while** loop.
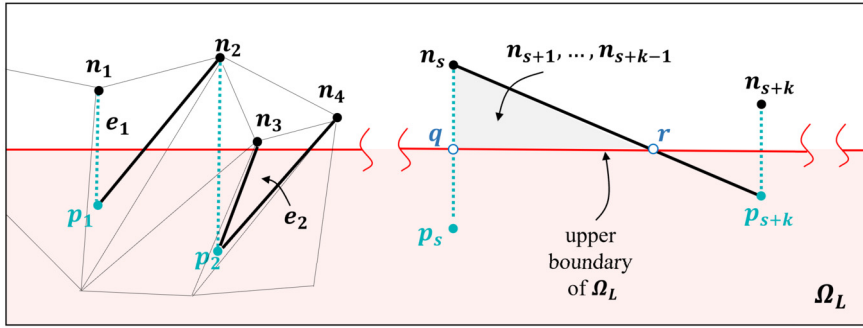
Fig. 6. Illustration of the proof (by contradiction) of Proposition 1 in 2D.

Proof. (For the 2D case.) We prove the proposition in 2D by contradiction, using some basic graph theory. If Algorithm 1 does not terminate after a finite number of iterations, there must be a set of ghost nodes for which the label function $\mathcal{L}$ remains 0. Let $\tilde{\mathbb{N}} \subset \mathbb{N}_g$ denote this set. We show by contradiction that $\tilde{\mathbb{N}} = \emptyset$.

Because of Steps 3 and 4 in Algorithm 1-2, the projection of any node in $\tilde{\mathbb{N}}$ on $\partial\Omega_L$ must be on the side boundary, which in 2D means the upper or lower boundary. Let $\tilde{\mathbb{N}}^{(u)}$ and $\tilde{\mathbb{N}}^{(l)}$ be the set of ghost nodes in $\tilde{\mathbb{N}}$ whose projection point is on the upper and lower boundary, respectively. Hence, $\tilde{\mathbb{N}} = \tilde{\mathbb{N}}^{(l)} \cup \tilde{\mathbb{N}}^{(u)}$. If $\tilde{\mathbb{N}} \neq \emptyset$, at least one of $\tilde{\mathbb{N}}^{(u)}$ and $\tilde{\mathbb{N}}^{(l)}$ is not empty.

Assume $\tilde{\mathbb{N}}^{(u)} \neq \emptyset$. For any node $\boldsymbol{n}_i \in \tilde{\mathbb{N}}^{(u)}$, let $\boldsymbol{e}_i \in \Omega^h$ denote the element in Ω^h that contains the image point, $\boldsymbol{p}_i$. Among the vertices of $\boldsymbol{e}_i$, at least one of them must be a node in $\tilde{\mathbb{N}}$, and is not $\boldsymbol{n}_i$. Otherwise, in Line 45 of Algorithm 1, $\boldsymbol{n}_i$ would have been populated, leading to $\mathcal{L}_i = 1$. The mesh resolution condition mentioned above further ensures that this node must be within $\tilde{\mathbb{N}}^{(u)}$. We refer to this node as a *patron* of $\boldsymbol{n}_i$. For example, in Fig. 6, $\boldsymbol{n}_2$ is a patron of $\boldsymbol{n}_1$; $\boldsymbol{n}_3$ and $\boldsymbol{n}_4$ are patrons of $\boldsymbol{n}_2$. In other words, each node in $\tilde{\mathbb{N}}^{(u)}$ must have at least one patron in $\tilde{\mathbb{N}}^{(u)}$. Because all the elements in Ω^h are triangles (and hence convex), if $\boldsymbol{n}_j$ is a patron of $\boldsymbol{n}_i$, the line segment $\boldsymbol{p}_i\boldsymbol{n}_j$ is entirely covered by element $\boldsymbol{e}_i$.

Now, we define a directed graph $\mathbb{G}(\tilde{\mathbb{N}}^{(u)}, \mathbb{E})$, using $\tilde{\mathbb{N}}^{(u)}$ as the set of vertices/nodes. The set of edges, $\mathbb{E}$, comprises all the *patronages* within $\tilde{\mathbb{N}}^{(u)}$, i.e.

$$\mathbb{E} = \{(\boldsymbol{n}_i, \boldsymbol{n}_j) \mid \boldsymbol{n}_i, \boldsymbol{n}_j \in \tilde{\mathbb{N}}^{(u)}, \boldsymbol{n}_j \text{ is a patron of } \boldsymbol{n}_i\}. \tag{43}$$

Because each node in $\tilde{\mathbb{N}}^{(u)}$ has at least one patron, the outdegree of each node is at least 1. We apply a basic theorem in graph theory: a directed graph in which every vertex has outdegree greater than or equal to 1 contains a directed cycle [61]. Let sequence

$$\mathbb{C} = \{\boldsymbol{n}_s, \boldsymbol{n}_{s+1}, \cdots, \boldsymbol{n}_{s+k}, \boldsymbol{n}_s\} \subset \tilde{\mathbb{N}}^{(u)} \tag{44}$$

denote the shortest directed cycle in $\mathbb{G}$. If $\mathbb{G}$ has multiple directed cycles of the minimum length, let $\mathbb{C}$ be any of them. Because the elements in mesh Ω^h are triangles, it is not possible for two nodes in $\tilde{\mathbb{N}}^{(u)}$ to be a patron of each other. Therefore, $\mathbb{G}$ cannot have any multiple edge. Obviously, it cannot have any self-loop either. Therefore, the length of $\mathbb{C}$ is
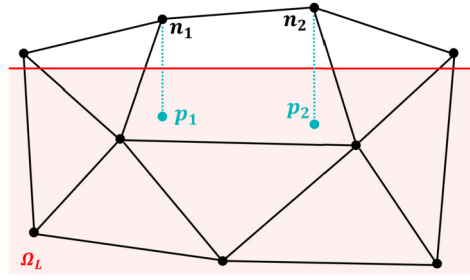
Fig. 7. An example in 2D showing that even if the embedded boundary is a straight line, the mirroring and interpolation method described in Algorithm 1 may still involve an infinite loop if the mesh has a non-simplex element. In this example, $\mathcal{L}_1$ and $\mathcal{L}_2$ will remain 0.

at least 3, i.e. $k \geq 2$ in (44). For each pair of nodes $\boldsymbol{n}_{s+i}$, $\boldsymbol{n}_{s+j}$ $(i < j)$ in $\mathbb{C}$, the corresponding elements $\boldsymbol{e}_{s+i}$, $\boldsymbol{e}_{s+j}$ must be different. Otherwise, $\{\boldsymbol{n}_s, \cdots, \boldsymbol{n}_{s+i}, \boldsymbol{n}_{s+j+1}, \cdots, \boldsymbol{n}_{s+k}, \boldsymbol{n}_s\}$ would be a shorter directed cycle.

In the following, we show that because the upper boundary of Ω_L is a straight line, a cycle like $\mathbb{C}$ cannot exist.

First, *any two of the line segments*

$$\boldsymbol{p}_s \boldsymbol{n}_{s+1}, \ \boldsymbol{p}_{s+1} \boldsymbol{n}_{s+2}, \ \cdots, \ \boldsymbol{p}_{s+k} \boldsymbol{n}_s$$

cannot intersect. Otherwise, the two different elements in mesh Ω^h that cover them would have to intersect and overlap.

Without loss of generality, let $\boldsymbol{n}_s$ be the node in $\mathbb{C}$ that is closest to the laser source, as shown in Fig. 6. Let point $\boldsymbol{q}$ be the intersection of $\boldsymbol{n}_s \boldsymbol{p}_s$ and the upper boundary of Ω_L, i.e. the projection point of $\boldsymbol{n}_s$. The line segment $\boldsymbol{p}_{s+k} \boldsymbol{n}_s$ must cross the upper boundary of Ω_L at a point that is farther from the laser source than $\boldsymbol{q}$.[2] Let $\boldsymbol{r}$ denote this point, as shown in Fig. 6.

All the other nodes in $\mathbb{C}$, namely $\boldsymbol{n}_{s+1}, \cdots, \boldsymbol{n}_{s+k-1}$, must be located within the triangle defined by $\boldsymbol{n}_s$, $\boldsymbol{q}$, and $\boldsymbol{r}$ as vertices. In Fig. 6, this triangle is shown as the gray, shaded area. Otherwise, if $\boldsymbol{n}_{s+i}$ is the first node in the sequence that is located outside of the triangle, then $\boldsymbol{p}_{s+i-1} \boldsymbol{n}_{s+i}$ would intersect $\boldsymbol{p}_{s+k} \boldsymbol{n}_s$.

Because $\boldsymbol{n}_{s+k-1}$ is inside the triangle, while $\boldsymbol{n}_{s+k}$ is outside and to the right, $\boldsymbol{p}_{s+k-1} \boldsymbol{n}_{s+k}$ has to intersect $\boldsymbol{p}_{s+k} \boldsymbol{n}_s$, which contradicts the statement above highlighted in italic text. Therefore, $\tilde{\mathbb{N}}^{(u)} = \emptyset$.

In the same way, we can prove $\tilde{\mathbb{N}}^{(l)} = \emptyset$. Hence, $\tilde{\mathbb{N}} = \tilde{\mathbb{N}}^{(u)} \bigcup \tilde{\mathbb{N}}^{(l)} = \emptyset$ $\quad \square$

Remark. One of the conditions of the proposition is that all the elements in Ω^h are simplices. Fig. 7 shows that when a 2D unstructured mesh has a quadrangle element, Algorithm 1 may not terminate due to an infinite loop. As recommended in Sec. 3.4, for non-Cartesian meshes, any non-simplex elements may be divided into simplices when updating the laser radiance at ghost nodes.

3.4.2. Order-of-accuracy analysis

The laser radiation equation, Eq. (23), can be written as

$$\mathcal{R}(L) \equiv \nabla \cdot (L\boldsymbol{s}) + \mu_\alpha(T)L = 0. \tag{45}$$

Similarly, its finite volume discretization, (30), can be written as

$$\mathcal{R}^h(L) \equiv \frac{1}{\|C_i\|} \sum_{j \in Nei(i)} A_{ij} L_{ij} (\boldsymbol{s}_{ij} \cdot \boldsymbol{n}_{ij}) + \mu_\alpha(T_i) L_i = 0, \tag{46}$$

where L_{ij} is calculated using the mean flux method, Eq. (31).

Let $\widetilde{L}(\boldsymbol{x})$ denote the solution of Eq. (45). We show that for a uniform Cartesian grid,

$$\mathcal{R}^h(\widetilde{L}) = (1 - 2\alpha)Ch + O(h^2) \tag{47}$$

at each node within Ω_L. Here, h denotes the character size of the control volume. In other words, the mean flux method is second-order accurate if $\alpha = 0.5$.

For simplicity of notation, we consider the 2D case. For an arbitrary node $\boldsymbol{n}_{i,j}$ inside Ω_L, let $L_{i,j}$ denote the numerical solution at this node, which is also the center of control volume $C_{i,j}$. Therefore,

---

[2] If there are multiple nodes in $\mathbb{C}$ that have the same, smallest distance to the laser source, at least one of them satisfies the requirement. Let that one be $\boldsymbol{n}_s$.
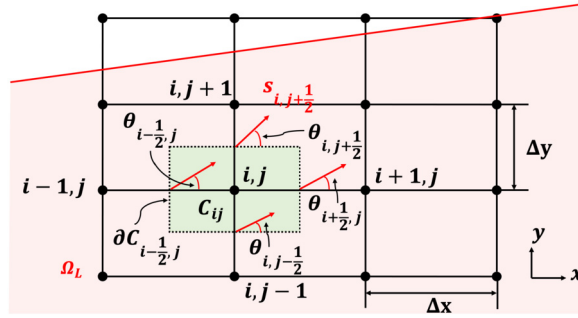
Fig. 8. 2D illustration of the finite volume method for the order-of-accuracy analysis.

$$\mathcal{R}^h(L_{i,j}) = \frac{1}{\Delta x}(\cos\theta_{i+\frac{1}{2},j}L_{i+\frac{1}{2},j} - \cos\theta_{i-\frac{1}{2},j}L_{i-\frac{1}{2},j}) + \frac{1}{\Delta y}(\sin\theta_{i,j+\frac{1}{2}}L_{i,j+\frac{1}{2}} - \sin\theta_{i,j-\frac{1}{2}}L_{i,j-\frac{1}{2}})$$
$$+ \mu_{\alpha(i,j)}L_{i,j} = 0, \tag{48}$$

where Δx and Δy denote the width of $C_{i,j}$ in x and y directions, respectively. θ denotes the angle between $\boldsymbol{s}$ and the x axis, and its subscript indicates the position where it is evaluated (Fig. 8).

Substituting Eq. (31) into Eq. (48) yields

$$\mathcal{R}^h(L_{i,j}) = \frac{1}{\Delta x}(\cos\theta_{i+\frac{1}{2},j}(\alpha L_{i,j} + (1-\alpha)L_{i+1,j}) - \cos\theta_{i-\frac{1}{2},j}(\alpha L_{i-1,j} + (1-\alpha)L_{i,j}))$$
$$+ \frac{1}{\Delta y}(\sin\theta_{i,j+\frac{1}{2}}(\alpha L_{i,j} + (1-\alpha)L_{i,j+1}) - \sin\theta_{i,j-\frac{1}{2}}(\alpha L_{i,j-1} + (1-\alpha)L_{i,j}))$$
$$+ \mu_{\alpha(i,j)}L_{i,j} = 0. \tag{49}$$

Substituting the exact solution $\widetilde{L}(\boldsymbol{x}_{i,j})$ into Eq. (49) yields

$$\mathcal{R}^h(\widetilde{L}(\boldsymbol{x}_{i,j})) = \frac{1}{\Delta x}(\cos\theta_{i+\frac{1}{2},j}(\alpha\widetilde{L}(\boldsymbol{x}_{i,j}) + (1-\alpha)\widetilde{L}(\boldsymbol{x}_{i+1,j})) - \cos\theta_{i-\frac{1}{2},j}(\alpha\widetilde{L}(\boldsymbol{x}_{i-1,j}) + (1-\alpha)\widetilde{L}(\boldsymbol{x}_{i,j})))$$
$$+ \frac{1}{\Delta y}(\sin\theta_{i,j+\frac{1}{2}}(\alpha\widetilde{L}(\boldsymbol{x}_{i,j}) + (1-\alpha)\widetilde{L}(\boldsymbol{x}_{i,j+1})) - \sin\theta_{i,j-\frac{1}{2}}(\alpha\widetilde{L}(\boldsymbol{x}_{i,j-1}) + (1-\alpha)\widetilde{L}(\boldsymbol{x}_{i,j})))$$
$$+ \mu_{\alpha(i,j)}\widetilde{L}(\boldsymbol{x}_{i,j}). \tag{50}$$

Expanding $\widetilde{L}$ and θ about $\boldsymbol{x}_{i,j}$ gives

$$\mathcal{R}^h(\widetilde{L}(\boldsymbol{x}_{i,j})) = \left(\cos\theta_{i,j}\frac{\partial\widetilde{L}}{\partial x} + \sin\theta_{i,j}\frac{\partial\widetilde{L}}{\partial y}\right) + \widetilde{L}(\boldsymbol{x}_{i,j})\left(\cos\theta_{i,j}\frac{\partial\theta}{\partial y} - \sin\theta_{i,j}\frac{\partial\theta}{\partial x}\right) + \mu_{\alpha(i,j)}\widetilde{L}(\boldsymbol{x}_{i,j})$$
$$+ \frac{1}{2}(1-2\alpha)\left(\cos\theta_{i,j}\Delta x\frac{\partial^2\widetilde{L}}{\partial x^2} + \sin\theta_{i,j}\Delta y\frac{\partial^2\widetilde{L}}{\partial y^2}\right)$$
$$+ \frac{1}{2}(1-2\alpha)\left(\Delta y\cos\theta_{i,j}\frac{\partial\widetilde{L}}{\partial y}\frac{\partial\theta}{\partial y} - \Delta x\sin\theta_{i,j}\frac{\partial\widetilde{L}}{\partial x}\frac{\partial\theta}{\partial x}\right) + O(\Delta x^2, \Delta y^2), \tag{51}$$

where all the derivatives are computed at $\boldsymbol{x}_{i,j}$. By Eq. (45),

$$\left(\cos\theta_{i,j}\frac{\partial\widetilde{L}}{\partial x} + \sin\theta_{i,j}\frac{\partial\widetilde{L}}{\partial y}\right) + \widetilde{L}(\boldsymbol{x}_{i,j})\left(\cos\theta_{i,j}\frac{\partial\theta}{\partial y} - \sin\theta_{i,j}\frac{\partial\theta}{\partial x}\right) + \mu_{\alpha(i,j)}\widetilde{L}(\boldsymbol{x}_{i,j}) = \mathcal{R}(\widetilde{L}(\boldsymbol{x}_{i,j})) = 0. \tag{52}$$

Substituting Eq. (52) into Eq. (51) yields

$$\mathcal{R}^h(\widetilde{L}(\boldsymbol{x}_{i,j})) = \frac{1}{2}(1-2\alpha)\left(\cos\theta_{i,j}\Delta x\frac{\partial^2\widetilde{L}}{\partial x^2} + \sin\theta_{i,j}\Delta y\frac{\partial^2\widetilde{L}}{\partial y^2} + \cos\theta_{i,j}\Delta y\frac{\partial\widetilde{L}}{\partial y}\frac{\partial\theta}{\partial y} - \sin\theta_{i,j}\Delta x\frac{\partial\widetilde{L}}{\partial x}\frac{\partial\theta}{\partial x}\right)$$
$$+ O(h^2), \tag{53}$$

where $h = \max(\Delta x, \Delta y)$. $\square$

If $\boldsymbol{n}_{i,j}$ is near the side boundary of Ω_L, some of its neighbors (i.e. $\boldsymbol{n}_{i\pm1,j}$, $\boldsymbol{n}_{i,j\pm1}$) may be ghost nodes. As an example, assume $\boldsymbol{n}_{i,j+1}$ is a ghost node. Based on Algorithm 1-3, the radiance at $\boldsymbol{n}_{i,j+1}$ is computed using the embedded boundary method, i.e.

$$L_{i,j+1} = \sum_{k=1}^{n_k} w_k L_k, \tag{54}$$

where n_k denotes the number of vertices of the element that contains the image of node $\boldsymbol{n}_{i,j+1}$. w_k is the weight associated with vertex k in linear interpolation. Thus, we have

$$L_{i,j+1} = \widetilde{L}(\boldsymbol{x}_{p_{i,j+1}}) + O(h^2), \tag{55}$$

where $\boldsymbol{x}_{p_{i,j+1}}$ is the coordinates of the image of node $\boldsymbol{n}_{i,j+1}$. Therefore, the embedded boundary method updates the values of L at ghost nodes up to second-order accuracy, which is equivalent to a first-order approximation of the symmetry boundary condition, Eq. (39).

Remarks.

- The analysis above can be easily extended to 3D, giving the same orders of accuracy for the finite volume method and the embedded boundary method.
- The analysis above assumes a Cartesian grid. In Section 4.1, we present a numerical order-of-accuracy analysis for 2D unstructured meshes. The results obtained from the numerical analysis are consistent with the findings obtained here.

3.5. Phase transition

The method of latent heat reservoir described in Sec. 2.4 is implemented in the coupled laser-fluid computational framework. At the end of each time step, for each control volume C_i in $\Omega_L \cap \Omega_0$, the liquid temperature T_i is obtained by Eq. (6). We compare it with T_{vap}, and there are three possibilities.

(a) If $T_i \leq T_{vap}$ and $\Lambda_i = 0$, no additional actions are taken.
(b) If $T_i \leq T_{vap}$ and $\Lambda_i > 0$, we use the latent heat stored here (i.e. Λ_i) to increase the local temperature up to T_{vap}. Specifically, let $e = e_{vap}$ be the solution of

$$T(\rho_i, e) = T_{vap}. \tag{56}$$

We update Λ_i and e_i as follows.

$$\Lambda_i = \Lambda_i - \min(e_{vap} - e_i, \ \Lambda_i), \tag{57}$$

$$e_i = e_i + \min(e_{vap} - e_i, \ \Lambda_i). \tag{58}$$

(c) If $T_i > T_{vap}$, we reduce T_i to T_{vap}, and move the excessive heat to the latent heat reservoir, Λ_i. Again, we solve Eq. (56) to obtain e_{vap}. Then, Λ_i and e_i are updated by

$$\Lambda_i = \Lambda_i + (e_i - e_{vap}), \tag{59}$$

$$e_i = e_i - (e_i - e_{vap}) = e_{vap}. \tag{60}$$

Next, we compare Λ_i and l to determine if phase transition should occur at node $\boldsymbol{n}_i$. If $\Lambda_i \geq l$, this control volume undergoes phase transition. The phase identification number $\mathcal{I}_i$ is changed to be 1, which identifies the vapor phase. The density ρ_i and velocity $\boldsymbol{V}_i$ in C_i remain unchanged. Λ_i is added to the enthalpy of the vapor, and the internal energy is updated by Eq. (26).

If $\Lambda_i < l$, but C_i undergoes phase change due to the motion of the liquid-vapor interface, the stored energy Λ_i is added to the internal energy, e_i.

4. Numerical experiments

4.1. Verification of the laser radiation solver

We present three test cases to assess the convergence and order of accuracy of the laser radiation solver, including the mean flux method presented in Sec. 3.3 and the embedded boundary method presented in Sec. 3.4.

Fig. 9 shows the setup of these test cases. In all the cases, a parallel Gaussian laser beam with power $P_0 = 560$ W is imposed. The use of a parallel beam allows us to derive the exact solution of the problem in closed-form expression. The laser source is placed at $x = 0$ mm, with a radius of 0.3 mm (i.e. -0.3 mm $\leq y \leq 0.3$ mm). The computational domain, Ω, has a length of 1.7 mm and a radius of 0.5 mm. Therefore, the upper and lower boundaries of the laser radiation domain, Ω_L, are embedded in Ω. In Tests 1 and 2, the entire computational domain is assumed to be filled with liquid water, with laser absorption coefficient $\mu_\alpha = 2.42$ mm^{-1} [13]. The waist radius of the laser beam (w_0) is set to 0.15 mm in Test 1
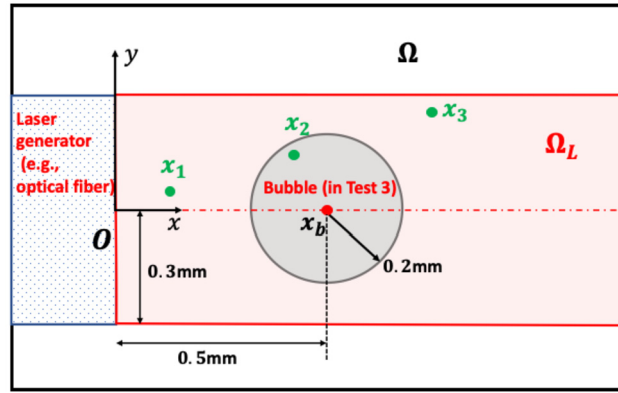
Fig. 9. Problem setup for the verification of the laser radiation solver.

Table 1
Meshes for the verification of the laser radiation solver.

Mesh	Characteristic edge length (mm)	Edge length variation		Number of nodes	Number of elements
		Max (mm)	Min (mm)		
1	0.025	0.0330	0.0188	1535	2892
2	0.0125	0.0161	0.0094	5974	11594
3	0.00625	0.0086	0.0047	23582	46458
4	0.003125	0.0046	0.0022	92083	182756
5	0.0015625	0.0025	0.00097	355091	707364
6	0.00078125	0.0012	0.00048	1399305	2793066

and 0.35 mm in Test 2. Therefore, the numerical result obtained from Test 2 would be more sensitive to errors induced by the embedded boundary method. In Test 3, the waist radius is set to be the same as in Test 2. In addition, we introduce a bubble within Ω_L with a radius of 0.2 mm. The fluid inside the bubble is assumed to be water vapor, with a laser absorption coefficient of 0.

Six unstructured triangular meshes with different resolutions are generated to discretize the computational domain, Ω. The number of elements increases from $2,892$ in Mesh 1 to $2,793,066$ in Mesh 6. Because these meshes are not uniform, the edges in each mesh do not have the same length. The characteristic edge length varies from 2.5×10^{-2} mm in Mesh 1 to 7.8125×10^{-4} mm in Mesh 6. Additional information about these meshes are presented in Table 1.

For each test case, different values of α (see Eq. (31)) between 0.5 and 1 are tested. For each value of α, six simulations are performed using the six different meshes. The numerical solutions of laser radiance (L) obtained with $\alpha = 0.5$ using the finest mesh are shown in Fig. 10. The laser radiance in Test 1 has a higher peak value than that in Test 2, and is also more focused. This can be explained by the difference in waist radius between the two test cases. In Test 3, the laser radiance remains constant within the bubble along the laser's propagation direction. This is because the laser absorption coefficient is set to 0 inside the bubble. In Tests 2 and 3, the laser radiance on the side boundary of Ω_L is clearly non-zero, and has a large gradient in the normal direction. Therefore, the embedded boundary method plays a significant role in these two cases.

To assess the convergence and order of accuracy of the numerical methods, we compare the numerical solutions with the exact solutions at three sensor points. The locations of these sensor points are marked in Fig. 9. Their coordinates (in mm) are $\boldsymbol{x}_1 : (0.1, \ 0.05)$, $\boldsymbol{x}_2 : (0.4, \ 0.15)$ and $\boldsymbol{x}_3 : (0.8, \ 0.25)$, respectively. Specifically, Sensor 1 is close to the laser source, in the upstream direction of the bubble (in Test 3). Sensor 2 is placed inside the bubble, and Sensor 3 near the (embedded) upper boundary of Ω_L.

At each sensor, the relative error is computed by

$$e(\boldsymbol{x}_i) = \frac{|L(\boldsymbol{x}_i) - \widetilde{L}(\boldsymbol{x}_i)|}{\widetilde{L}(\boldsymbol{x}_i)}, \ i = 1, 2, 3, \tag{61}$$

where $L(\boldsymbol{x}_i)$ is the numerical solution at $\boldsymbol{x}_i$, calculated by linearly interpolating the simulation results within the element that contains the point. For the parallel beam used in these cases, the exact solution of laser radiance at these sensor points are given by
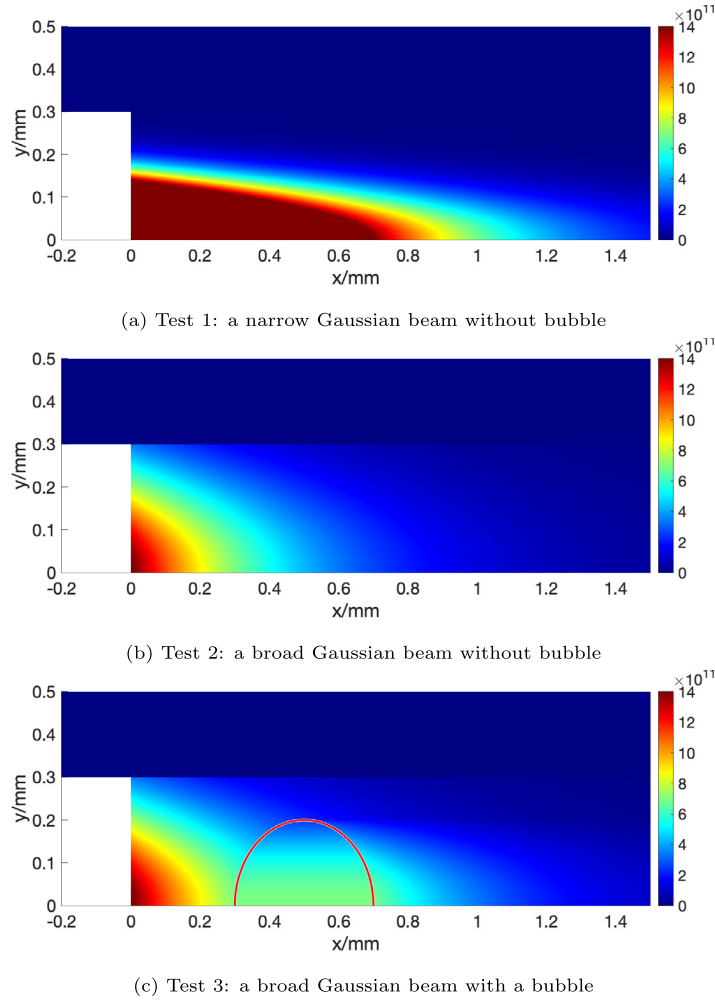
(a) Test 1: a narrow Gaussian beam without bubble

(b) Test 2: a broad Gaussian beam without bubble

(c) Test 3: a broad Gaussian beam with a bubble

Fig. 10. Numerical solution of laser radiance (unit: g/s^3) obtained using the finest mesh. (For interpretation of the colors in the figure(s), the reader is referred to the web version of this article.)

$$\begin{cases} \widetilde{L}(\boldsymbol{x}_i) = \widetilde{L}(\boldsymbol{x}_{s_i}) \exp(-\mu_\alpha |\boldsymbol{x}_i - \boldsymbol{x}_{s_i}|), \quad i = 1, 3, \\ \widetilde{L}(\boldsymbol{x}_2) = \begin{cases} \widetilde{L}(\boldsymbol{x}_{s_2}) \exp(-\mu_\alpha |\boldsymbol{x}_2 - \boldsymbol{x}_{s_2}|), & \text{Tests 1 and 2,} \\ \widetilde{L}(\boldsymbol{x}_{s_2}) \exp(-\mu_\alpha |\boldsymbol{x}_{b_2} - \boldsymbol{x}_{s_2}|), & \text{Test 3,} \end{cases} \end{cases} \tag{62}$$

where $\boldsymbol{x}_{s_i}$, $i = 1, 2, 3$ is the projection point of $\boldsymbol{x}_i$ on the laser source plane, and the radiance there can be calculated by Eq. (25). $\boldsymbol{x}_{b_2}$ is the left intersection point between the laser beam that passes through $\boldsymbol{x}_2$ and the bubble surface.

The relative errors at the three sensor points are shown in Figs. 11, 12, and 13 for the three test cases, respectively. The horizontal axis is the characteristic mesh edge length, h, in a log scale. The vertical axis shows the relative error, e, also in a log scale. Therefore, the slope of the straight lines that fit the errors obtained with different meshes gives the order of accuracy obtained at each sensor point. For reference, straight lines with slopes 1 and 2 are also shown in each figure.

For Test 1 (Fig. 11), we observe a first-order convergence rate for $\alpha = 1.0$ and a second-order convergence rate for $\alpha = 0.5$ at all the three sensors. This is consistent with the analytical result derived in Sec. 3.4 (cf. Eq. (47)), despite that the derivation was performed for a Cartesian mesh, while the numerical tests employed unstructured triangular meshes. In Test 2, and for $\alpha = 0.5$, second-order accuracy is still obtained at all the sensors, including the one that is close to the embedded boundary, i.e. $\boldsymbol{x}_3$ (Fig. 12). This indicates that the embedded boundary method presented in Sec. 3.4 retains second-order accuracy in the interior of the laser radiation domain.

In Test 3, even with $\alpha = 0.5$, we only observe a first-order convergence rate at the three sensor points (Fig. 13). A comparison with Test 2 suggests that this accuracy order reduction is caused by the discontinuity of solution at the bubble surface, which results from the discontinuity of the absorption coefficient, μ_α. It is noteworthy that when $\alpha = 0.5$, the laser radiance at any node is influenced by neighbors in both upstream and downstream directions. Therefore, the errors made at the bubble surface also influence the order of accuracy at Sensor 1, which is in the upstream direction of the bubble.
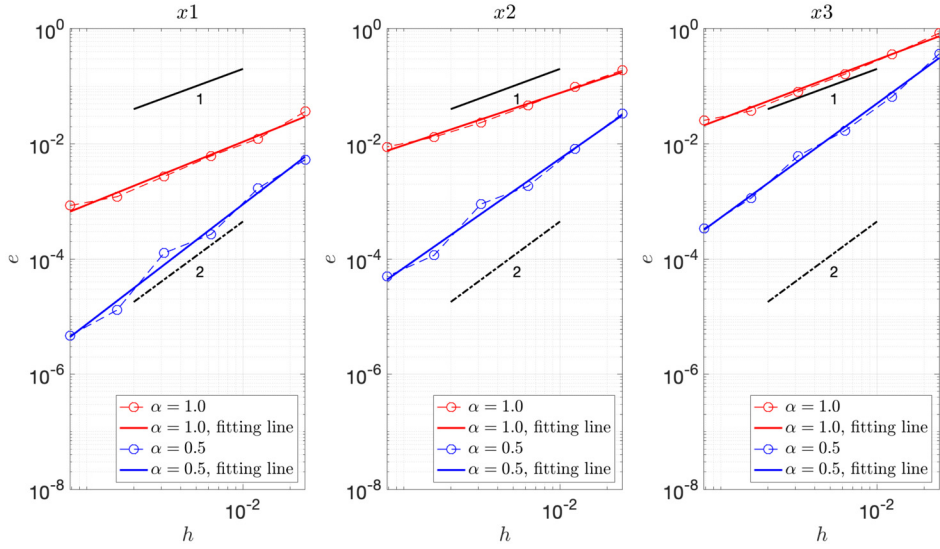
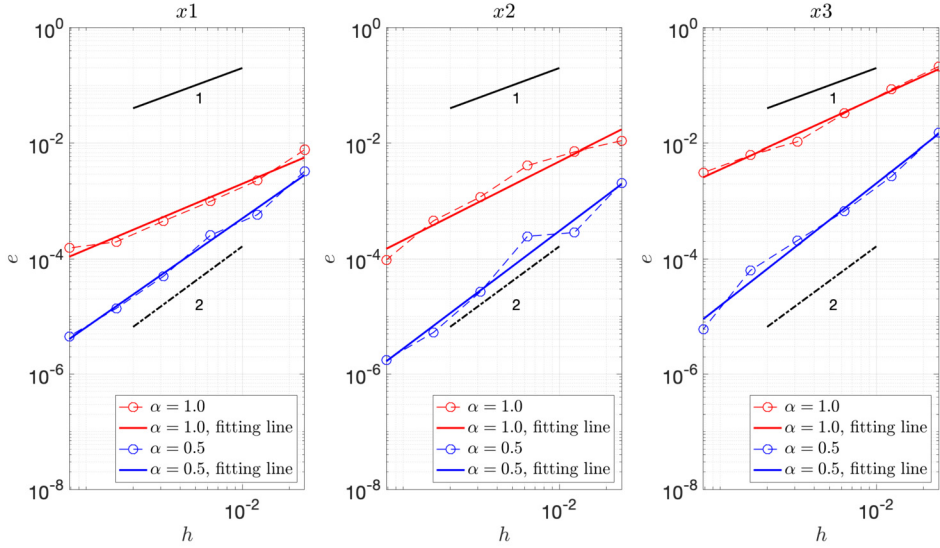**Fig. 11.** Relative error in laser radiance at three sensor points: Test 1.

Fig. 12. Relative error in laser radiance at three sensor points: Test 2.

4.2. Verification of the level set equation solver

To verify the convergence of the numerical methods for solving the level set equation (Sec. 3.2), we present two benchmark problems that have been widely used in previous studies (e.g., [48,49]).

First, we apply the level set method to track a circle that undergoes large, vortex-induced distortion. The computational domain is defined by $\Omega = [0, 1] \times [0, 1]$. Initially, a circle with radius $r = 0.15$ is centered at $(x, y) = (0.5, 0.75)$. A solenoidal velocity field is specified to deform the circle into a slender spiral tape, and then restore it to its original configuration. The velocity field is time-dependent, given by:

$$\begin{cases} u = 2\sin^2(\pi x)\sin(\pi y)\cos(\pi y)\cos(\pi t/t_f), \\ v = -2\sin(\pi x)\cos(\pi x)\sin^2(\pi y)\cos(\pi t/t_f), \end{cases} \tag{63}$$

where $t_f = 8.0$ is the final time, when the circle returns to its original configuration.

This test problem is solved using three different methods, including

(a) the full-domain level set method without reinitialization,
(b) the full-domain level set method with reinitialization performed at every time step, and
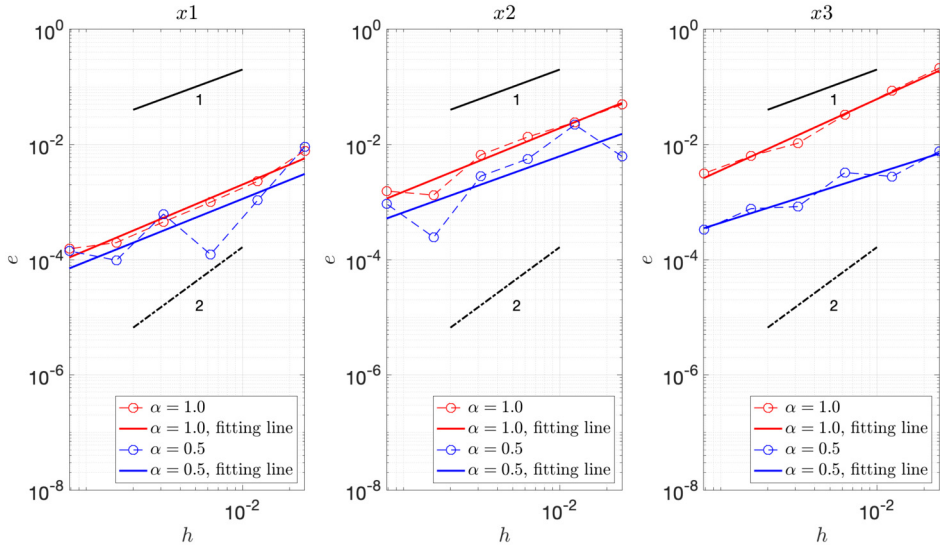
Fig. 13. Relative error in laser radiance at three sensor points: Test 3.
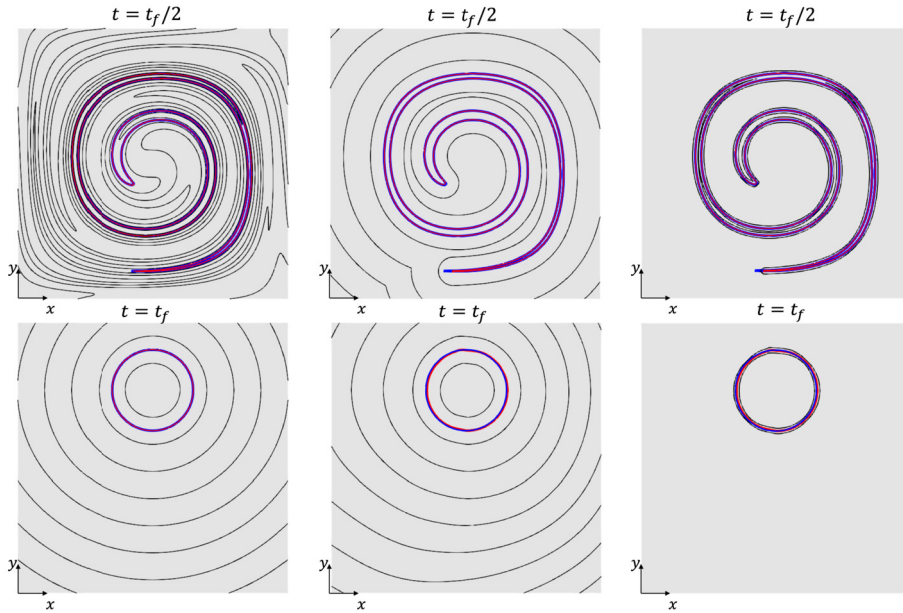
Fig. 14. Vortex-induced distortion of a circle: Numerical results obtained using (a) the full-domain level set method without reinitialization (left column), (b) the full-domain level set method with reinitialization after each time step (middle column), and (c) the narrow-band level set method with reinitialization after each time step (right column). In each sub-figure, the red curve is the numerical solution of the zero level set. The blue curve is a reference solution generated using Method (a) on a 2048^2-cell mesh.

 (c) the localized level set method (bandwidth: 10) with reinitialization performed at every time step.

All the three methods are tested on a 1024^2-cell mesh. To generate a reference solution, Method (a) is used to perform a simulation on a 2048^2-cell mesh. The numerical solutions at $t = t_f/2$ and $t = t_f$ are visualized in Fig. 14.

At $t = t_f/2$, the maximum distortion of the circle is reached. The 0 level set obtained by Method (a) agrees well with the reference solution. However, by examining the non-zero level sets, it is clear that the level set function ϕ is no longer a signed distance function. The 0 level sets obtained by Methods (b) and (c) are similar to each other. Overall, they are also in good agreement with the reference solution. But it is evident that the sharp end of the spiral-shaped surface is smeared (and hence shorter). Because of reinitialization, the level set function ϕ is maintained as a signed distance function in both cases. At $t = t_f$, the 0 level set obtained by all the three methods matches well with the reference solution.
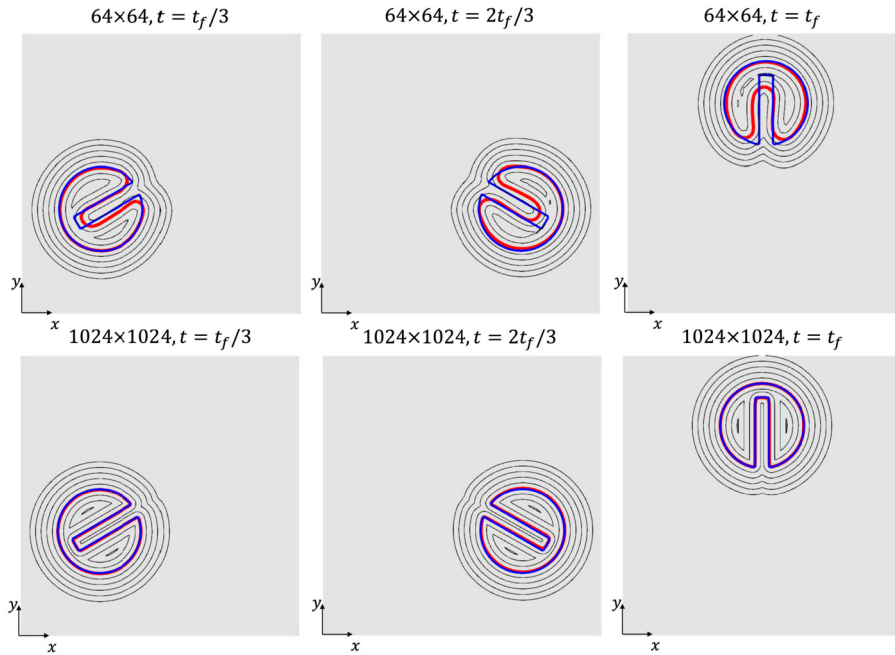
Fig. 15. Rotation of a slotted disk: Numerical solutions obtained using two meshes (64×64 and 1024×1024) at three different time instants. In each sub-figure, the red curve marks the numerical solution of the 0 level set, i.e. the surface of the slotted disk. The blue curve shows the exact solution.

This benchmark problem shows that the localized level set method (i.e. Method (c)) provides similar accuracy compared to the full-domain level set method (i.e. Methods (a) and (b)). For problems involving laser-induced vaporization, the reinitialization of level set needs to be performed frequently in order to capture local phase transitions, which renders Method (a) unsuitable. Between Methods (b) and (c), the latter can be significantly faster in sequential computations, because it uses a smaller computational domain. Nonetheless, due to the possibility of load unbalance, this advantage may become less obvious in parallel computations where some subdomains may be largely or entirely within the computation bandwidth. In subsequent numerical tests, Method (c) is used to solve the level set equation.

Next, the rotation of a slotted disk is simulated to assess the performance of the localized level set method in tracking sharp corners. The computational domain is a square, defined by $\Omega = [0, \ 100] \times [0, \ 100]$. A disk with radius $r = 15$ is initially placed in the upper part of Ω, centered at $(x, y) = (50, 75)$. A 5×25 slot is cut out of the disk, thereby creating several sharp corners that make the problem challenging for implicit interface tracking methods. The slotted disk is forced to rotate about the center of Ω by a time-independent solenoidal velocity field, $(u, \ v) = (\pi/314(50 - y), \ \pi/314(x - 50))$. By design, the disk should return to its initial position at time $t_f = 628$.

For this problem, the level set function is reinitializatied every 10 time steps. The results obtained using a 64^2-cell mesh and a 1024^2-cell mesh are shown in Fig. 15. Specifically, the solutions at three time instants, namely $t_f/3$, $2t_f/3$ and t_f, are plotted. The results on the coarser mesh show that the 0 level set matches the exact solution in the curved parts of the slotted disk. But the sharp corners are gradually smeared. However, with the mesh refined, the 0 level set converges to the exact solution at all the time instants.

4.3. Verification of level set reinitialization after phase transition

As described in Sec. 3.5, when local phase transitions are detected, we update the sign of ϕ to track the new liquid-vapor interface, then restore it to a distance function by solving the reinitialization equation, Eq. (17). Here, we present one numerical test to demonstrate this method.

In this test, the computational domain is 3D, defined by $\Omega = [-0.5 \ \text{mm}, \ 0.5 \ \text{mm}] \times [-0.5 \ \text{mm}, \ 0.5 \ \text{mm}] \times [0 \ \text{mm}, \ 0.5 \ \text{mm}]$. The boundary with $z = 0$ mm is set to be a symmetry boundary. Initially, the domain is assumed to be occupied entirely by the liquid phase, without a liquid-vapor interface. After one time step (3.45×10^{-9} s), a spherical region centered at the origin of the domain, with radius $r = 0.1$ mm, is assumed to undergo phase transition. In the second time step, at the nodes within the aforementioned spherical region, ϕ is set to a small negative value, comparable to the local element size. Then, the level set reinitialization equation is solved to convert ϕ into a signed-distance function.

This test problem is solved on four meshes with different resolutions, specifically, from $50 \times 50 \times 25$ cells to $400 \times 400 \times 200$ cells. Fig. 16 shows the numerical result of ϕ at three stages, namely (a) before phase transition, (b) after phase transition, but before level set reinitialization, and (c) after level set reinitialization.
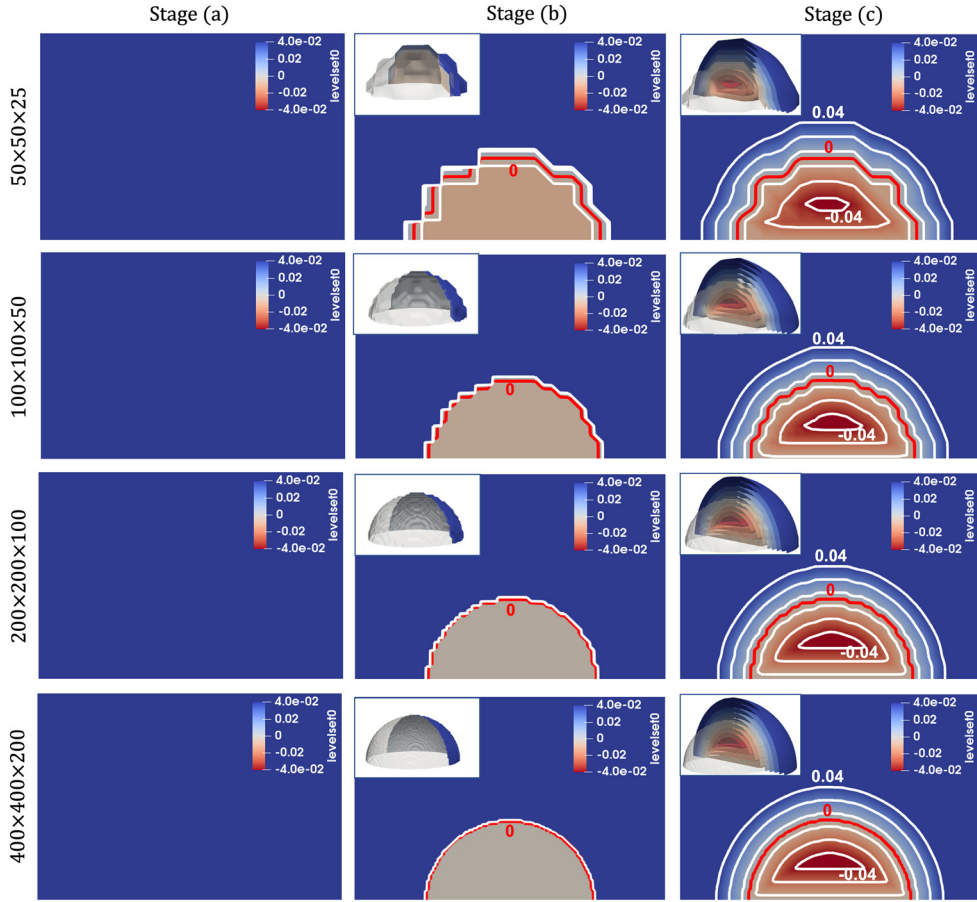
Fig. 16. Reinitialization of the level set function after phase transition.

At Stage (a), there is only one phase, and the value of ϕ is a constant positive value in the entire domain. At Stage (b), ϕ has the correct sign at every node, but it is not a signed distance function. At Stage (c), ϕ has both the correct sign and the correct absolute value that corresponds to the shorted distance from each node to the liquid-vapor interface. It can also be observed that as the mesh gets refined, the numerical solution of the 0 level set converges to a hemisphere, which is the true solution.

4.4. Laser-induced cavitation: a broad Gaussian beam

We apply the coupled laser-fluid solver presented in Fig. 3 and Sec. 3 to simulate the formation and expansion of a bubble induced by a broad Gaussian laser beam. Fig. 17 shows the setup of this problem. Specifically, we consider a cylindrical domain with a radius of 6 mm and a length of 12 mm, as shown in Fig. 17a. Initially, the domain is filled with water with density $\rho_0 = 0.001$ g/mm^3, velocity $v_0 = 0$ mm/s, pressure $p_0 = 100$ kPa, and temperature $T_0 = 273.15$ K.

A Holmium:YAG laser with a wavelength of 2.12×10^{-3} mm is simulated. The laser source is placed at $x = -0.5$ mm, as shown in Fig. 17b. The radius of the laser fiber is set by $r = 0.1825$ mm, following the lab experiments presented in [14]. The beam is assumed to have a divergence of $7.5°$. The spatial profile of laser radiance at the source is shown in Fig. 17c. A Gaussian distribution is assumed, with waist radius $w_0 = 0.12$ mm. The temporal profile of the laser power (P_0) is shown in Fig. 17d. Specifically, the power grows rapidly from 0 to 2.854 kW within 0.2 μs. This peak power is maintained for a period of 9.8 μs. Then, it vanishes rapidly within 0.2 μs. The laser absorption coefficient, μ_α, is set to 2.42 mm^{-1} for liquid water [13] and 0.001 mm^{-1} for the vapor.

In this simulation, liquid water is modeled by the stiffened gas EOS with $\gamma_0 = 6.12$ and $p_{c0} = 343$ MPa (see Eq. (4)), following [30]. Water vapor is modeled by the perfect gas EOS, with $\gamma_1 = 1.34$ (Eq. (5)). The specific heat at constant pressure, c_p, is set to 4.2×10^9 mm^2/(s^{2}K) for liquid water and 2.0×10^9 mm^2/(s^{2}K) for water vapor. The vaporization temperature and latent heat are set by $T_{\mathrm{vap}} = 373.15$ K and $l = 2256.4$ J/g, respectively.

The simulation is carried out on a two-dimensional mesh, leveraging the cylindrical symmetry of the problem. The mesh is Cartesian, with approximately 338, 000 elements. In the most refined region, the characteristic element size is approximately 2.5×10^{-3} mm. To track the vapor bubble, the localized level set method is used with a bandwidth of 6
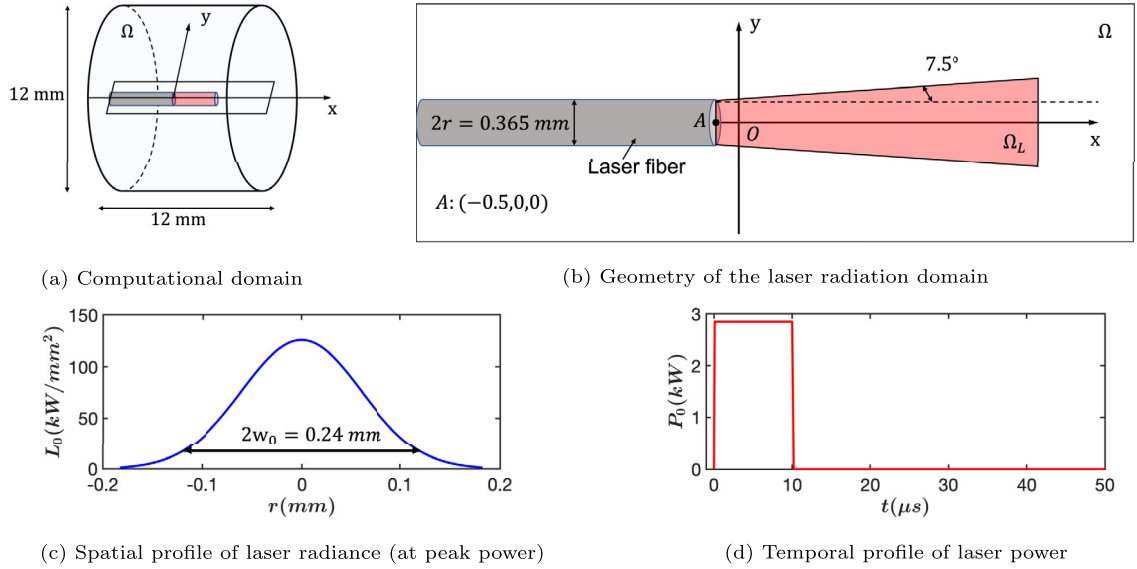
(a) Computational domain

(b) Geometry of the laser radiation domain

(c) Spatial profile of laser radiance (at peak power)

(d) Temporal profile of laser power

Fig. 17. Cavitation induced by a broad Gaussian beam: Problem setup.
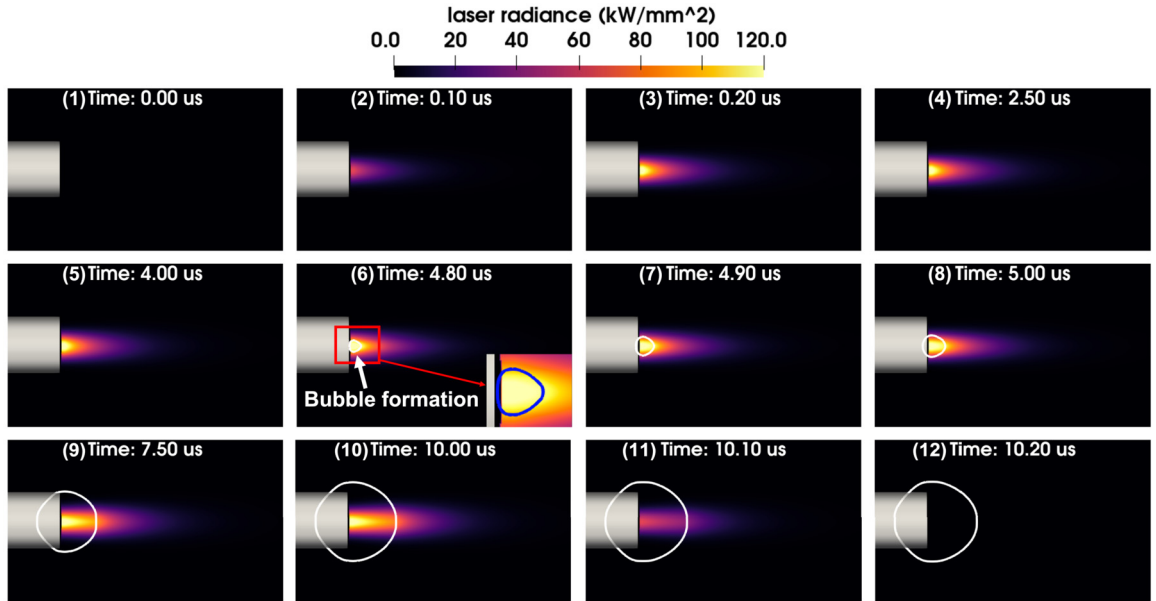

Fig. 18. Cavitation induced by a broad Gaussian beam: Laser radiance at different time instants.

elements on each side of the interface. A second-order Runge-Kutta method is used to advance both the fluid governing equations and the level set equation in time. The time step size is around 3×10^{-4} µs. The simulation is terminated at $t = 50$ µs. Results obtained from the simulation include the time-histories of the density, velocity, pressure, and temperature fields of the two-phase fluid flow, the level set function ϕ that tracks the liquid-vapor interface, and the laser radiance field.

Fig. 18 shows the result of laser radiance at twelve time instants during the simulation. The laser fiber is added to the images for ease of interpretation. It is not modeled in the simulation. The overall evolution of laser radiance is consistent with the temporal profile of laser power shown in Fig. 17d. More specifically, Sub-figures (1), (2), and (3) capture the rapid ramp-up of laser power in the first 0.2 µs. Because of the absorption by water, laser radiance decreases along the propagation direction. In Sub-figures (3) to (5), the laser radiance field remains the same, because the source power is constant during this time interval. At 4.8 µs, vaporization occurs, as a small bubble appears in front of the laser fiber. This bubble can be observed clearly in the inset image in Sub-figure (6). Sub-figures (7) to (10) capture the initial expansion of the vapor bubble, caused by the high internal pressure. It can be observed that laser radiance decreases much slower inside
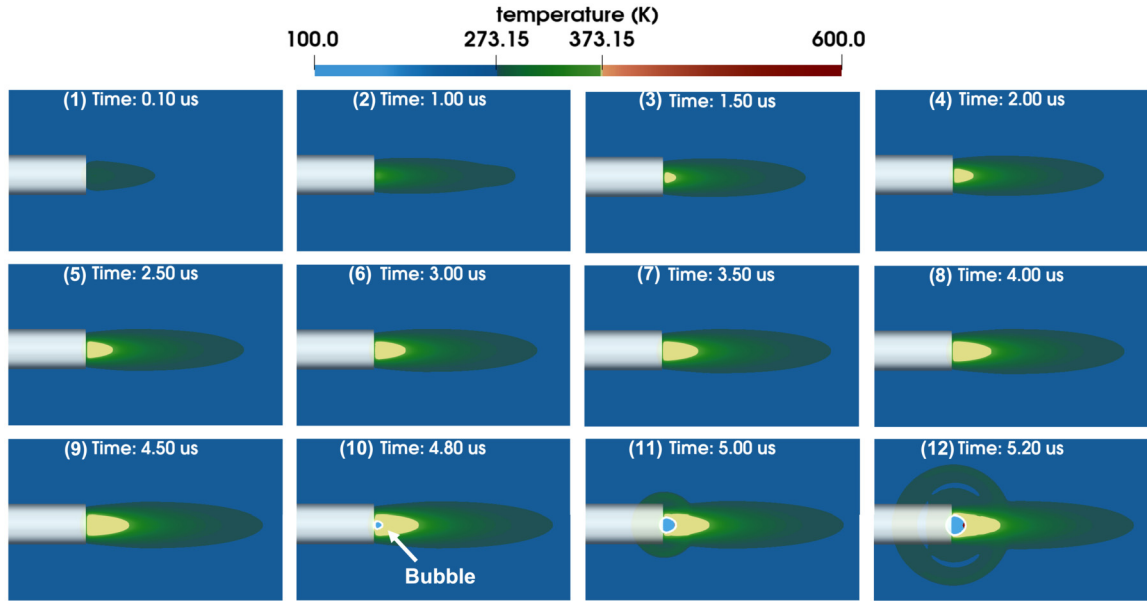
Fig. 19. Cavitation induced by a broad Gaussian beam: Temperature field at different time instants.

the bubble, due to the lower absorption coefficient. For example, in Sub-figures (5) and (10), the laser source power is the same. Nonetheless, the hot zone (i.e. the region with high radiance) is clearly longer in the latter. In other words, the bubble has created a channel that allows laser energy to be delivered further. This phenomenon is sometimes referred to as the Moses effect [14,21,50,51].

Fig. 19 presents the temperature field at twelve time instants, showing the absorption of laser by the liquid and the resulting vaporization. In Sub-figures (1), (2), and (3), it is clear that water temperature is highest at the tip of the laser fiber, along its central axis. The temperature decreases in radial directions due to the Gaussian beam profile. It also decreases in the axial direction, for which there are two reasons. First, the absorption of laser by water leads to the decay of laser radiance in the axial direction. Second, the laser beam used in this simulation has a 7.5° divergence angle. At around 1.5 μs, the specified vaporization temperature, T_{vap}, is reached at the tip of the laser fiber, which appears as a yellow region in Sub-figure (3). The temperature in this region remains constant until 4.8 μs, when vaporization occurs. During this time, the absorbed laser energy is used to overcome the intermolecular bonds in liquid water. In the simulation, it is stored in the latent heat reservoir (Λ) described in Sec. 3.5. Meanwhile, the region where T_{vap} has been reached expands in both axial and radial directions. At 4.8 μs (Sub-figure (10)), the latent heat of vaporization has been accumulated at the tip of the laser fiber. At this point, phase transition occurs, and the latent heat is converted into the enthalpy of the vapor phase. As a result, the vapor bubble has a high internal pressure. The pressure jump across the bubble surface leads to the emission of a shock wave, which can be seen in Sub-figures (11) and (12).

Fig. 20 presents the pressure field at sixteen time instants between 0 and 50 μs. The formation and expansion of the vapor bubble are both captured in these images. Sub-figure (1) is taken at the same time as Fig. 19(1), which shows the rapid increase of thermodynamic pressure due to the absorption of laser energy. An outgoing shock wave is emitted from the high pressure zone, which is captured in Sub-figure(2). Subsequently, Sub-figures (3) and (4) show that as the shock wave travels outward, the pressure in front of the laser fiber decreases. Sub-figure (5) is taken at the time when vaporization occurs. The sudden release of latent heat leads to a dramatic increase of pressure inside the vapor bubble, exceeding 10^8 Pa. The pressure outside the bubble is less than 10^5 Pa. This significant pressure jump leads to the emission of an outgoing shock wave, captured in Sub-figures (6), (7), and (8). The pressure jump also propels the bubble to expand, which is captured in Sub-figures (6) through (16). At 50 μs (Sub-figure (16)), the bubble evolves into a teardrop shape around the central axis of the laser beam.

The velocity field at the same time instants is visualized in Fig. 21. In Sub-figures (1) through (4), it can be observed that due to the absorption of laser energy, the water in front of the laser fiber flows outward. From Sub-figure (2) to (4), the velocity decreases gradually, as the laser radiance stops growing. After the formation of vapor bubble, the velocity around the bubble surface increases dramatically, which reflects the bubble's expansion. Notably, the magnitude of fluid velocity is higher at the front of the bubble (i.e. the 3 o'clock direction in the images) compared to other regions. This difference gradually drives the bubble to grow into a teardrop shape. The same shape has been observed in laboratory experiments. For example, Fig. 22 shows the setup of an experiment using the same type of laser, as well as a bubble image captured by high-speed photography [14].
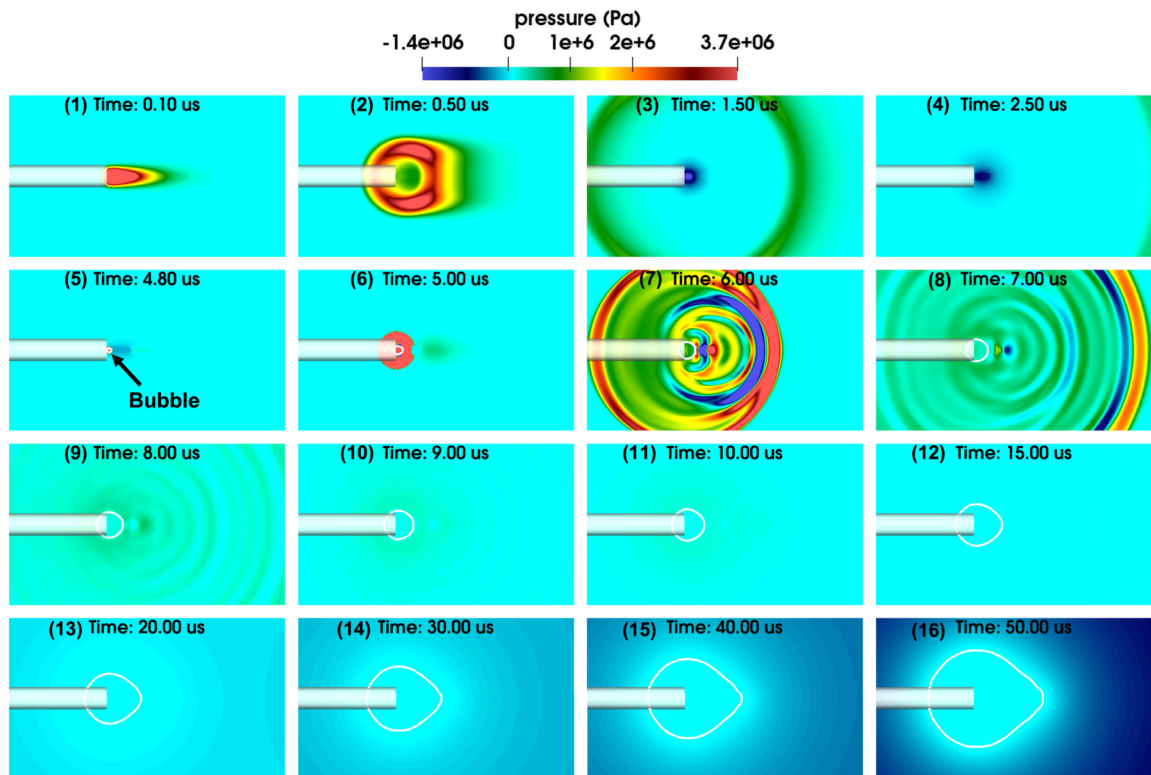
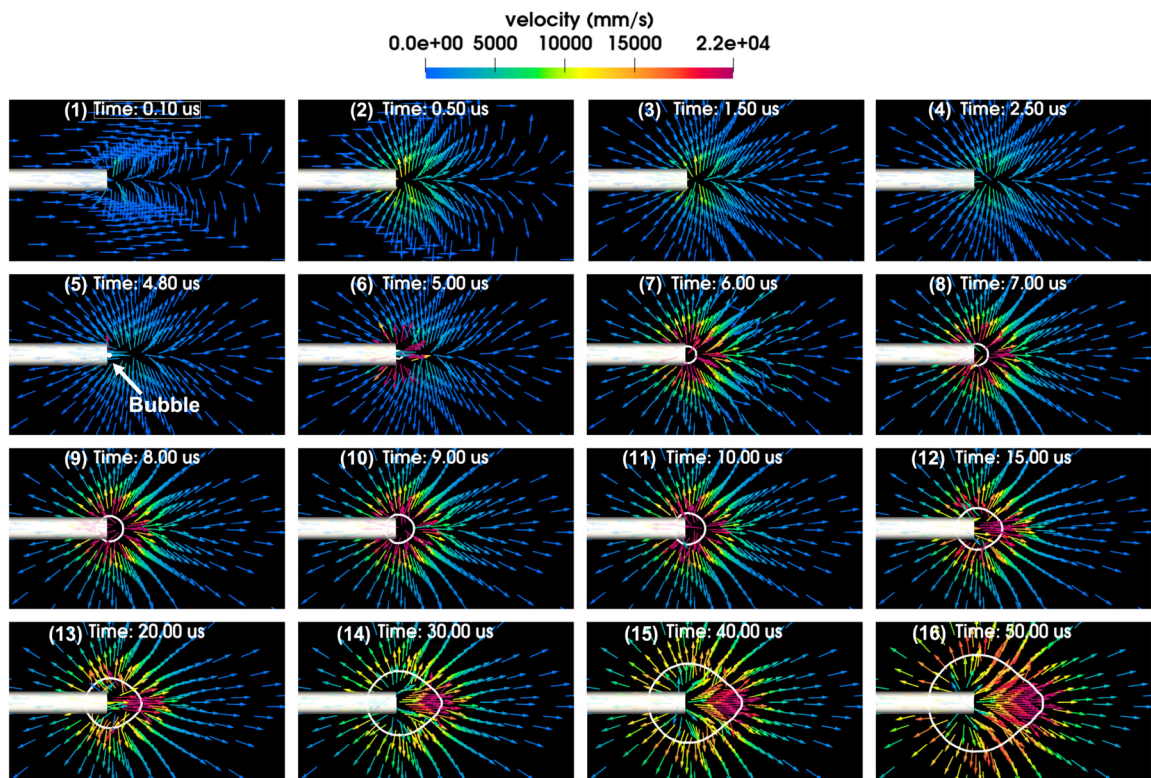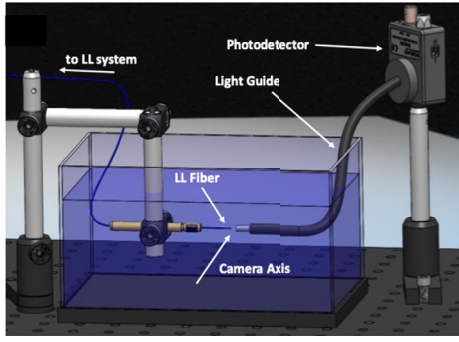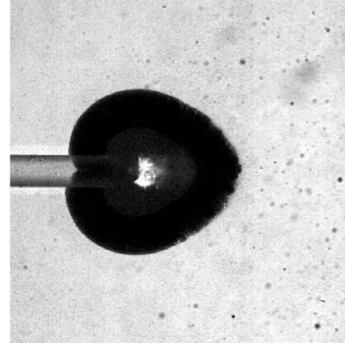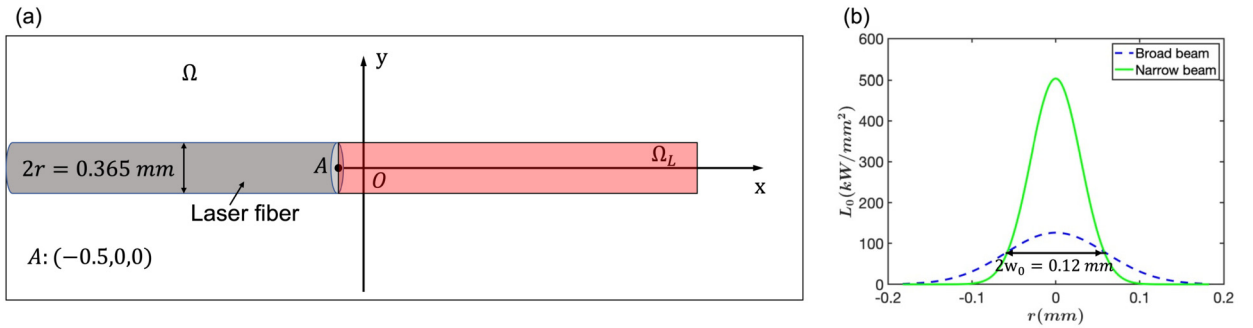**Fig. 20.** Cavitation induced by a broad Gaussian beam: Pressure field at different time instants.

Fig. 21. Cavitation induced by a broad Gaussian beam: Velocity field at different time instants.

(a) Setup of experiment

(b) Vapor bubble captured by high-speed photography

Fig. 22. A teardrop-shaped vapor bubble observed in a laboratory experiment of laser-induced cavitation [14].

Fig. 23. Cavitation induced by a narrow Gaussian beam: Problem setup. (a) Geometry of the laser radiation domain. (b) Spatial profile of laser radiance (at peak power).

4.5. Laser-induced cavitation: a narrow Gaussian beam

To demonstrate the potential use of the computational method for parametric studies, we simulate cavitation induced by a narrower laser beam. The same setup described in Sec. 4.4 is adopted, except that the waist radius of the Gaussian beam is reduced by a factor of 2 to 0.06 mm, and the angle of divergence is reduced to 0° (Fig. 23).

Fig. 24 shows the laser radiance field at twelve time instants. In comparison with Fig. 18, the laser beam is clearly narrower. Also, the maximum radiance, which is achieved along the central axis of the beam, is higher compared to the previous case. In this case, vaporization starts at 1.3 μs, much earlier than in the previous case. This moment is captured by Sub-figure (5). After this time, vaporization continues in the axial direction. Therefore, the evolution of the vapor bubble is driven both by the high pressure inside the bubble and the continuous phase transition. This is another major difference from the previous case. In Sub-figures (6) through (12), it can be observed that the bubble gradually grows into an elongated, conical shape. Because of the elongated bubble, the Moses effect is more significant in this case, as shown in Sub-figures (7) through (10).

Fig. 25 shows the temperature field at twelve time instants. Compared with the previous case (Fig. 19), several differences are clearly evident. First, the temperature around the central axis of the laser beam rises at a higher speed. As a result, the vaporization temperature, T_{vap}, is reached at 0.4 μs, earlier than 1.5 μs in the previous case. Also, the latent heat required for vaporization is also achieved at an earlier time, that is, 1.3 μs versus 4.8 μs. The expansion of the initial bubble is slower than the increase of internal energy in front of the bubble. Therefore, vaporization continues in the axial direction, which leads to an elongated bubble.

Fig. 26 shows the pressure field at sixteen time instants. Up to the time of vaporization (i.e. 1.3 μs), the main features exhibited in the pressure field are similar to those observed in the previous case. In particular, an outward going shock wave is captured in Sub-figures (1)-(4). Sub-figure(4) is taken at the time of vaporization, when a small, high pressure bubble appears right in front of the laser fiber. The shock wave induced by the pressure jump across bubble surface is captured in Sub-figure (5). A major difference from the previous case (cf. Fig. 20) is that the continuation of vaporization in the axial direction leads to the emission of new shock waves at the tip of the bubble. These shock waves are captured in Sub-figures (6) through (10). At 10.2 μs, laser radiation stops. Afterwards, vaporization also stops, and the bubble continues to grow due to the inertial effect. At the end of the simulation (50 μs), an elongated bubble is observed. This type of elongated bubbles have also been captured in laboratory experiments using high-speed photography. For example, see Fig. 2 in [19] and Fig. 7 in [21].
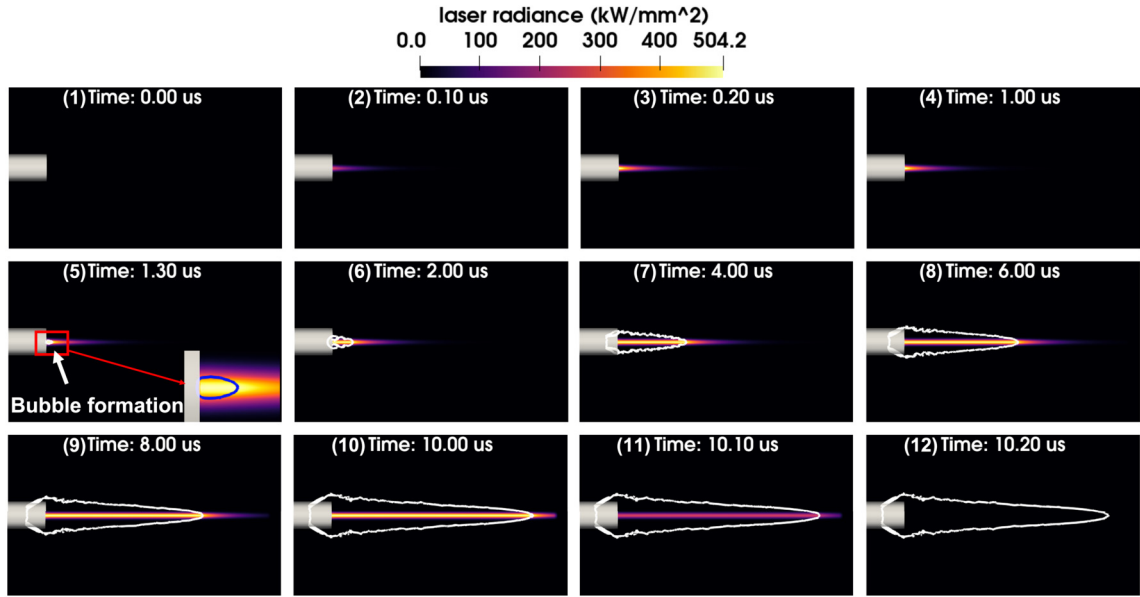
Fig. 24. Cavitation induced by a narrow Gaussian beam: Laser radiance at different time instants.
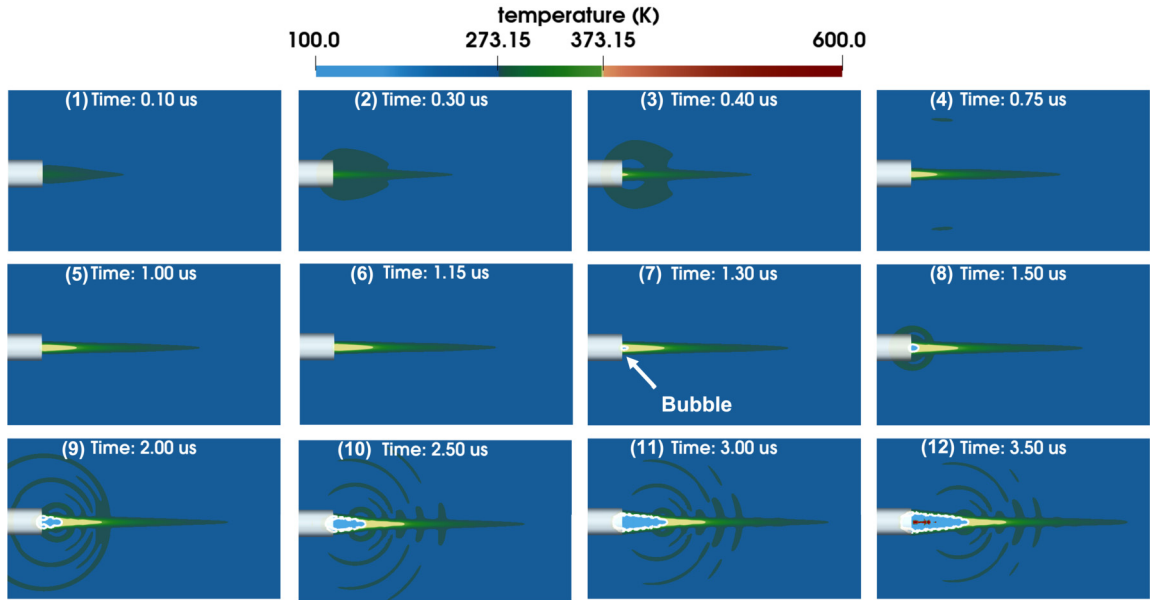

Fig. 25. Cavitation induced by a narrow Gaussian beam: Temperature field at different time instants.

Fig. 27 presents the velocity field at the same time instants as in Fig. 26. As expected, high velocity can be observed around and within the elongated vapor bubble. Notably, the velocity is not much higher at the tip of the bubble (i.e. the 3 o'clock direction) than in other regions (e.g., the upper and lower sides). This indicates that the bubble's elongation in the axial direction is primarily driven by the continuation of vaporization.

5. Summary

A computational method for simulating cavitation induced by long-pulsed laser is presented. The definition of "long-pulsed" varies for different laser technologies and applications. In this paper, it refers to laser pulses with a duration that is comparable to or longer than the acoustic time scale. In this context, the processes of laser radiation, phase transition (i.e. vaporization), and bubble/fluid dynamics overlap both in time and in space. The computational method is designed to simulate these processes simultaneously using a physical model that accounts for their dependencies (Fig. 3).
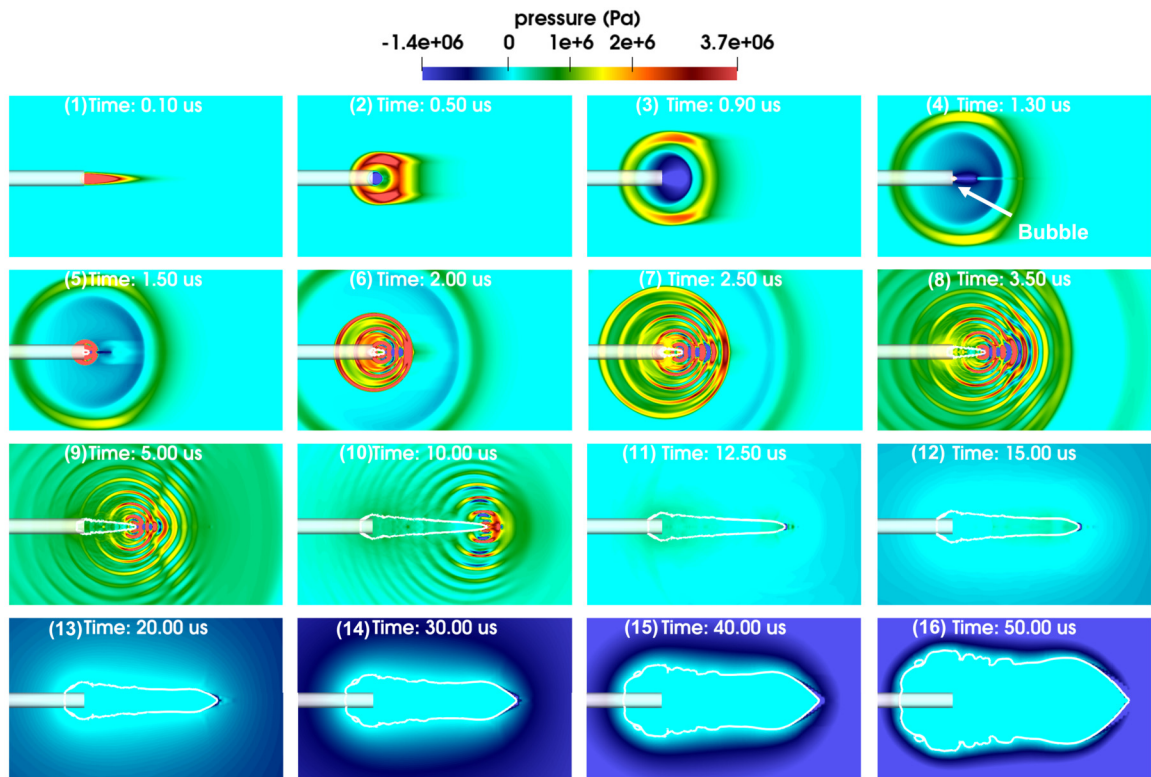
Fig. 26. Cavitation induced by a narrow Gaussian beam: Pressure field at different time instants.
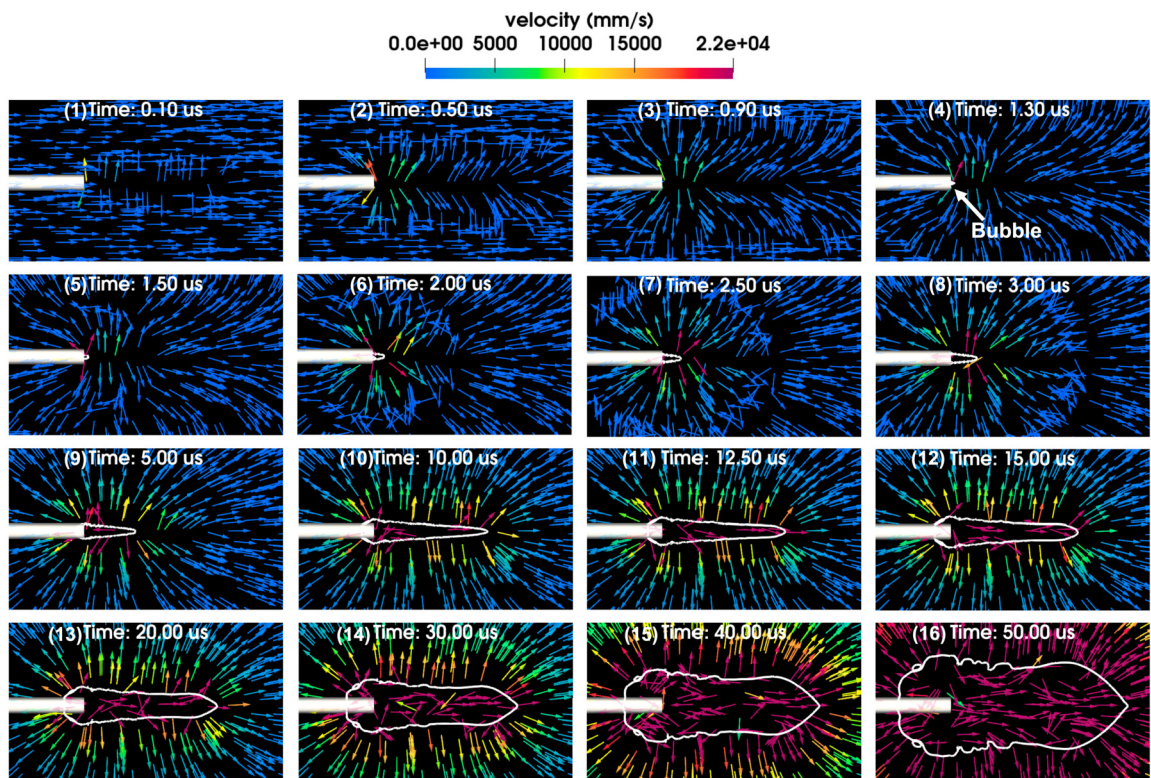

Fig. 27. Cavitation induced by a narrow Gaussian beam: Velocity field at different time instants.

An embedded boundary method is presented to couple the fluid dynamics equations with the laser radiation equation, allowing the latter to be solved on the same finite volume mesh constructed for the former. This mesh generally does not resolve the boundaries of the laser radiation domain. As a result, special treatments are needed to avoid spurious radiation fluxes across the side boundary of the laser radiation domain. The basic idea of the embedded boundary method is to set the laser radiance at selected nodes outside the laser domain (i.e. ghost nodes) to be equal to the linearly interpolated radiance values at their images inside the domain, thereby imposing a symmetry boundary condition. The existence and uniqueness of solution is proved for the 2D case, leveraging the special geometry of laser domains.

An implicit interface tracking method is presented to track the dynamics of the cavitation bubble(s). This method can be viewed as an extension of the conventional level set method that accounts for the formation and expansion of bubbles due to phase transitions. During a simulation, local vaporization is detected using a method of latent heat reservoir, which keeps track of the increase of intermolecular potential energy prior to phase transition. At any time step, if vaporization is detected at some nodes in the mesh, a level set reinitialization equation is solved to restore the level set function to a signed distance function with respect to the expanded vapor bubble.

Several numerical experiments are presented to demonstrate and assess the computational method. The convergence and accuracy properties of the numerical techniques are first assessed using simple academic problems. The predictive capability of the computational method is demonstrated using two realistic simulations. It is shown that even with relatively simple material models — perfect and stiffened gas EOS, linear temperature laws, constant vaporization temperature and latent heat — and without *ad hoc* calibration, the computational method is able to capture several important phenomena in laser-induced cavitation, including non-spherical, beam-dependent bubble expansion (Figs. 21 and 27), shock waves (Figs. 20 and 26), and the Moses effect (Figs. 18 and 24).

CRediT authorship contribution statement

Xuning Zhao: Conceptualization, Methodology, Code development, Verification and Validation, Writing – original draft preparation, Reviewing and editing. **Wentao Ma:** Methodology, Code development, Writing – reviewing and editing. **Kevin Wang:** Conceptualization, Methodology, Code development, Writing – original draft preparation, Reviewing and editing.

Declaration of competing interest

The authors declare the following financial interests/personal relationships which may be considered as potential competing interests: Xuning Zhao, Wentao Ma, Kevin Wang report financial support was provided by National Science Foundation under Award CBET-1751487. Wentao Ma, Kevin Wang report financial support was provided by Office of Naval Research under Award N00014-19-1-2102. Xuning Zhao, Kevin Wang report financial support was provided by National Institutes of Health under Award 2R01-DK052985-24A1.

Data availability

Data will be made available on request.

Acknowledgement

References

[1] A. Vogel, W. Lauterborn, R. Timm, Optical and acoustic investigations of the dynamics of laser-produced cavitation bubbles near a solid boundary, J. Fluid Mech. 206 (1989) 299–338.

[2] Y. Tomita, P. Robinson, R. Tong, J. Blake, Growth and collapse of cavitation bubbles near a curved rigid boundary, J. Fluid Mech. 466 (2002) 259–283.

[3] A.N. Hellman, K.R. Rau, H.H. Yoon, S. Bae, J.F. Palmer, K.S. Phillips, N.L. Allbritton, V. Venugopalan, Laser-induced mixing in microfluidic channels, Anal. Chem. 79 (12) (2007) 4484–4492.

[4] S. Le Gac, E. Zwaan, A. van den Berg, C.-D. Ohl, Sonoporation of suspension cells with a single cavitation bubble in a microfluidic confinement, Lab Chip 7 (12) (2007) 1666–1672.

[5] G. Wang, J. Santiago, M. Mungal, B. Young, S. Papademetriou, A laser induced cavitation pump, J. Micromech. Microeng. 14 (7) (2004) 1037.

[6] L.R. Sklar, C.T. Burnett, J.S. Waibel, R.L. Moy, D.M. Ozog, Laser assisted drug delivery: a review of an evolving technology, Lasers Surg. Med. 46 (4) (2014) 249–262.

[7] I. Chida, K. Okazaki, S. Shima, K. Kurihara, Y. Yuguchi, I. Sato, Underwater cutting technology of thick stainless steel with YAG laser, in: First International Symposium on High-Power Laser Macroprocessing, vol. 4831, SPIE, 2003, pp. 453–458.

[8] A. Kruusing, Underwater and water-assisted laser processing: part 2—etching, cutting and rarely used methods, Opt. Lasers Eng. 41 (2) (2004) 329–352.

[9] A. Kruusing, Underwater and water-assisted laser processing: part 1—general features, steam cleaning and shock processing, Opt. Lasers Eng. 41 (2) (2004) 307–327.

[10] M. She, D. Kim, C.P. Grigoropoulos, Liquid-assisted pulsed laser cleaning using near-infrared and ultraviolet radiation, J. Appl. Phys. 86 (11) (1999) 6519–6524.

[11] A. Vogel, W. Hentschel, J. Holzfuss, W. Lauterborn, Cavitation bubble dynamics and acoustic transient generation in ocular surgery with pulsed neodymium: YAG lasers, Ophthalmology 93 (10) (1986) 1259–1269.

[12] A. Vogel, R. Engelhardt, U. Behnle, U. Parlitz, Minimization of cavitation effects in pulsed laser ablation illustrated on laser angioplasty, Appl. Phys. B 62 (2) (1996) 173–182.

[13] N.M. Fried, P.B. Irby, Advances in laser technology and fibre-optic delivery systems in lithotripsy, Nat. Rev. Urol. 15 (9) (2018) 563–573.

[14] D.S. Ho, D. Scialabba, R.S. Terry, X. Ma, J. Chen, G.N. Sankin, G. Xiang, R. Qi, G.M. Preminger, M.E. Lipkin, et al., The role of cavitation in energy delivery and stone damage during laser lithotripsy, J. Endourol. 35 (6) (2021) 860–870.

[15] M.M. Elhilali, S. Badaan, A. Ibrahim, S. Andonian, Use of the moses technology to improve holmium laser lithotripsy outcomes: a preclinical study, J. Endourol. 31 (6) (2017) 598–604.

[16] J. Chen, D.S. Ho, G. Xiang, G. Sankin, G.M. Preminger, M.E. Lipkin, P. Zhong, Cavitation plays a vital role in stone dusting during short pulse holmium: YAG laser lithotripsy, J. Endourol. (2021).

[17] C.E. Brennen, Cavitation in medicine, Interface Focus 5 (5) (2015) 20150022.

[18] T. Juhasz, G.A. Kastis, C. Suárez, Z. Bor, W.E. Bron, Time-resolved observations of shock waves and cavitation bubbles generated by femtosecond laser pulses in corneal tissue and water, Lasers Surg. Med. 19 (1) (1996) 23–31.

[19] M. Mohammadzadeh, J.M. Mercado, C.-D. Ohl, Bubble dynamics in laser lithotripsy, J. Phys. Conf. Ser. 656 (2015) 012004, IOP Publishing.

[20] H.-j. Jang, M.-a. Park, F.V. Sirotkin, J.J. Yoh, Laser-induced microjet: wavelength and pulse duration effects on bubble and jet generation for drug injection, Appl. Phys. B 113 (3) (2013) 417–421.

[21] J.W. Blanken, R.M. Verdaasdonk, Cavitation as a working mechanism of the Er, Cr: YSGG laser in endodontics: a visualization study, J. Oral Laser Appl. 7 (2) (2007).

[22] H. Lin, B.D. Storey, A.J. Szeri, Inertially driven inhomogeneities in violently collapsing bubbles: the validity of the Rayleigh–Plesset equation, J. Fluid Mech. 452 (2002) 145–162.

[23] J.M. Carroll, M.L. Calvisi, L.K. Lauderbaugh, Dynamical analysis of the nonlinear response of ultrasound contrast agent microbubbles, J. Acoust. Soc. Am. 133 (5) (2013) 2641–2649.

[24] M. Warnez, E. Johnsen, Numerical modeling of bubble dynamics in viscoelastic media with relaxation, Phys. Fluids 27 (6) (2015) 063103.

[25] S. Zhang, J.H. Duncan, G.L. Chahine, The final stage of the collapse of a cavitation bubble near a rigid wall, J. Fluid Mech. 257 (1993) 147–181.

[26] E. Klaseboer, C. Turangan, S.W. Fong, T.G. Liu, K.C. Hung, B.C. Khoo, Simulations of pressure pulse–bubble interaction using boundary element method, Comput. Methods Appl. Mech. Eng. 195 (33–36) (2006) 4287–4302.

[27] Q. Wang, M. Mahmud, J. Cui, W.R. Smith, A. Walmsley, Numerical investigation of bubble dynamics at a corner, Phys. Fluids 32 (5) (2020) 053306.

[28] E. Johnsen, T. Colonius, Numerical simulations of non-spherical bubble collapse, J. Fluid Mech. 629 (2009) 231–262.

[29] K.G. Wang, Multiphase fluid-solid coupled analysis of shock-bubble-stone interaction in shockwave lithotripsy, Int. J. Numer. Methods Biomed. Eng. 33 (10) (2017) e2855.

[30] S. Cao, G. Wang, O. Coutier-Delgosha, K. Wang, Shock-induced bubble collapse near solid materials: effect of acoustic impedance, J. Fluid Mech. 907 (2021).

[31] R. Saurel, F. Petitpas, R. Abgrall, Modelling phase transition in metastable liquids: application to cavitating and flashing flows, J. Fluid Mech. 607 (2008) 313–350.

[32] P.J. Zwart, A.G. Gerber, T. Belamri, et al., A two-phase flow model for predicting cavitation dynamics, in: Fifth International Conference on Multiphase Flow, Yokohama, Japan, vol. 152, 2004.

[33] A. Main, X. Zeng, P. Avery, C. Farhat, An enhanced fiver method for multi-material flow problems with second-order convergence rate, J. Comput. Phys. 329 (2017) 141–172.

[34] C. Farhat, A. Rallu, S. Shankaran, A higher-order generalized ghost fluid method for the poor for the three-dimensional two-phase flow computation of underwater implosions, J. Comput. Phys. 227 (16) (2008) 7674–7700.

[35] C. Farhat, J.-F. Gerbeau, A. Rallu, Fiver: a finite volume method based on exact two-phase Riemann problems and sparse grids for multi-material flows with large density jumps, J. Comput. Phys. 231 (19) (2012) 6360–6379.

[36] K.G. Wang, P. Lea, C. Farhat, A computational framework for the simulation of high-speed multi-material fluid–structure interaction problems with dynamic fracture, Int. J. Numer. Methods Eng. 104 (7) (2015) 585–623.

[37] O. Rouzaud, J. Hylkema, J.-L. Verant, L. Tesse, Development of the pharaon platform and onera numerical solvers for gas radiation, in: Radiation of High Temperature Gases in Atmospheric Entry, vol. 533, 2003, pp. 181–188.

[38] J. Amaya, O. Cabrit, D. Poitou, B. Cuenot, M. El Hafi, Unsteady coupling of Navier–Stokes and radiative heat transfer solvers applied to an anisothermal multicomponent turbulent channel flow, J. Quant. Spectrosc. Radiat. Transf. 111 (2) (2010) 295–301.

[39] A. Habibi, B. Merci, G.J. Heynderickx, Impact of radiation models in CFD simulations of steam cracking furnaces, Comput. Chem. Eng. 31 (11) (2007) 1389–1406.

[40] R. Löhner, J.R. Cebral, F.E. Camelli, S. Appanaboyina, J.D. Baum, E.L. Mestreau, O.A. Soto, Adaptive embedded and immersed unstructured grid techniques, Comput. Methods Appl. Mech. Eng. 197 (25–28) (2008) 2173–2197.

[41] R. Mittal, H. Dong, M. Bozkurttas, F. Najjar, A. Vargas, A. Von Loebbecke, A versatile sharp interface immersed boundary method for incompressible flows with complex boundaries, J. Comput. Phys. 227 (10) (2008) 4825–4852.

[42] A. O'Brien, M. Bussmann, A volume-of-fluid ghost-cell immersed boundary method for multiphase flows with contact line dynamics, Comput. Fluids 165 (2018) 43–53.

[43] S. Cao, A. Main, K.G. Wang, Robin-Neumann transmission conditions for fluid-structure coupling: embedded boundary implementation and parameter analysis, Int. J. Numer. Methods Eng. 115 (5) (2018) 578–603.

[44] S. Cao, G. Wang, K.G. Wang, A spatially varying Robin interface condition for fluid-structure coupled simulations, Int. J. Numer. Methods Eng. 122 (19) (2021) 5176–5203.

[45] D. Peng, B. Merriman, S. Osher, H. Zhao, M. Kang, A pde-based fast local level set method, J. Comput. Phys. 155 (2) (1999) 410–438.

[46] M. Sussman, P. Smereka, S. Osher, A level set approach for computing solutions to incompressible two-phase flow, J. Comput. Phys. 114 (1) (1994) 146–159.

[47] F. Gibou, R. Fedkiw, S. Osher, A review of level-set methods and some recent applications, J. Comput. Phys. 353 (2018) 82–109.

[48] D. Hartmann, M. Meinke, W. Schröder, Differential equation based constrained reinitialization for level set methods, J. Comput. Phys. 227 (14) (2008) 6821–6845.

[49] D. Hartmann, M. Meinke, W. Schröder, The constrained reinitialization equation for level set methods, J. Comput. Phys. 229 (5) (2010) 1514–1535.

[50] E. Ventimiglia, O. Traxer, What is moses effect: a historical perspective, J. Endourol. 33 (5) (2019) 353–357.

[51] J. Isner, R. Clarke, A. Katzir, D. Gal, S. DeJesus, K. Halaburka, Transmission characteristics of individual wavelengths in blood do not predict ability to accomplish laser ablation in a blood field-inferential evidence for the moses effect, in: Circulation, vol. 74, Amer. Heart Assoc., 7272 Greenville Avenue, Dallas, TX 75231-4596, 1986, p. 361.

[52] M.F. Modest, Radiative Heat Transfer, Academic Press, 2013.

[53] J.R. Howell, M.P. Mengüç, K. Daun, R. Siegel, Thermal Radiation Heat Transfer, CRC Press, 2020.

[54] A.J. Welch, M.J. Van Gemert, et al., Optical-Thermal Response of Laser-Irradiated Tissue, vol. 2, Springer, 2011.

[55] D. Yang, M.C. Converse, D.M. Mahvi, J.G. Webster, Expanding the bioheat equation to include tissue internal water evaporation during heating, IEEE Trans. Biomed. Eng. 54 (8) (2007) 1382–1388.

[56] S. Blauth, F. Hübner, C. Leithäuser, N. Siedow, T.J. Vogl, Mathematical modeling of vaporization during laser-induced thermotherapy in liver tissue, J. Math. Ind. 10 (1) (2020) 1.

[57] W. Ma, X. Zhao, C. Gilbert, K. Wang, Computational analysis of bubble-structure interactions in near-field underwater explosion, Int. J. Solids Struct. (2022) 111527.

[58] B. Van Leer, Towards the ultimate conservative difference scheme. V. A second-order sequel to Godunov's method, J. Comput. Phys. 32 (1) (1979) 101–136.

[59] D.Z. Huang, D. De Santis, C. Farhat, A family of position- and orientation-independent embedded boundary methods for viscous flow and fluid–structure interaction problems, J. Comput. Phys. 365 (2018) 74–104.

[60] D. Joseph, M. El Hafi, R. Fournier, B. Cuenot, Comparison of three spatial differencing schemes in discrete ordinates method using three-dimensional unstructured meshes, Int. J. Therm. Sci. 44 (9) (2005) 851–864.

[61] V. Chvátal, E. Szemerédi, Short cycles in directed graphs, J. Comb. Theory, Ser. B 35 (3) (1983) 323–327.